



Natural Resources  
Canada

Ressources naturelles  
Canada

**GEOLOGICAL SURVEY OF CANADA  
OPEN FILE 8593**

**Kitasu Hill: a Late-Pleistocene volcano,  
Swindle Island, British Columbia**

**J.M. Bednarski and T.S. Hamilton**

**2019**

**Canada** 



## **GEOLOGICAL SURVEY OF CANADA OPEN FILE 8593**

### **Kitasu Hill: a Late-Pleistocene volcano, Swindle Island, British Columbia**

**J.M. Bednarski<sup>1</sup> and T.S. Hamilton<sup>1</sup>**

<sup>1</sup>Geological Survey of Canada, 9860 West Saanich Road, Sidney, British Columbia V8L 4B2

**2019**

© Her Majesty the Queen in Right of Canada, as represented by the Minister of Natural Resources, 2019

Information contained in this publication or product may be reproduced, in part or in whole, and by any means, for personal or public non-commercial purposes, without charge or further permission, unless otherwise specified.

You are asked to:

- exercise due diligence in ensuring the accuracy of the materials reproduced;
- indicate the complete title of the materials reproduced, and the name of the author organization; and
- indicate that the reproduction is a copy of an official work that is published by Natural Resources Canada (NRCan) and that the reproduction has not been produced in affiliation with, or with the endorsement of, NRCan.

Commercial reproduction and distribution is prohibited except with written permission from NRCan. For more information, contact NRCan at [nrcan.copyrightdroitdauteur.nrcan@canada.ca](mailto:nrcan.copyrightdroitdauteur.nrcan@canada.ca).

Permanent link: <https://doi.org/10.4095/321052>

This publication is available for free download through GEOSCAN (<https://geoscan.nrcan.gc.ca/>).

#### **Recommended citation**

Bednarski, J.M. and Hamilton, T.S., 2019. Kitasu Hill: a Late-Pleistocene volcano, Swindle Island, British Columbia; Geological Survey of Canada, Open File 8593, 59 p. <https://doi.org/10.4095/321052>

Publications in this series have not been edited; they are released as submitted by the author.

## **GSC Open File 8593**

# **Kitasu Hill a Late-Pleistocene volcano, Swindle Island, British Columbia**

Jan Bednarski and Tark Hamilton

Pacific Geoscience Centre, Geological Survey of Canada–Pacific, 9860 W. Saanich Road, Sidney, BC V8L 4B2

### **Abstract**

Kitasu Hill is a small volcano on an outer island of coastal of British Columbia and is one of a group of the four late Quaternary-aged cinder cones peripheral to Milbanke Sound. The cones coincide with major structural lineaments in the area, but their relationship with these fault zones is unknown. Kitasu volcano was examined in detail by high resolution lidar topography and by paleomagnetic, geochemical and petrographic analyses on a limited number of field samples. An elevated platform of brecciated alkaline basalt and pillow lava forms the base of Kitasu volcano. The platform is straight-edged, abruptly terminating at ~80 m above sea level (asl) and is partially overlain by a well-preserved cinder cone reaching 233 m asl with two smaller cones nested within the main crater. Stratigraphy shows that parts of the volcanic platform is underlain by hyaloclastite containing a mixture of locally sourced basaltic material and ~20% mineral grains and glacial erratic cobbles from Coast Mountain sources. The sediment characteristics and overall morphology of the volcanic platform intimates that Kitasu volcano is a tuya with the initial eruption taking place in a subglacial setting during the waning stage of the last glaciation between 14.5 and 12.5 ka BP (radiocarbon years ago). Geomorphology and petrography, showing the preservation of glass and olivine in volcanic sediment, suggest that Kitasu Hill is predominantly a monogenetic depositional feature with little or no reworking or redeposition. The final pyroclastic eruptions took place sometime after 12.3 ka BP, based on the postglacial relative sea level history of the region. It is concluded that the Milbanke cones likely erupted near the end of the last glaciation rather than during postglacial time like previously thought. Coincidentally, during Late Pleistocene deglaciation the four cones were positioned similarly with respect to the retreating ice sheet and thus may have undergone similar glacially induced crustal stresses and erosion. We propose that the ice sheet mostly eroded two of the four Milbanke cones previously reported as erosional remnants, whereas Helmet Peak, the second best preserved cone, was partly eroded by south-flowing ice in Mathieson Channel. Kitasu Hill lies within the unceded territory of the Kitasoo/Xai'Xais First Nation.

## Introduction

Kitasu Hill (*pronounced “Kititsoo”*) is a small volcano on southern Swindle Island, one of the outer islands of coastal British Columbia (Fig. 1). This report presents the results of a site

defines the south shore of Swindle Island and Laredo Channel (Principe-Laredo shear zone; Nelson, 2011b). The relationship of the volcano to the lineament is unknown, but the Kitasu cone is one of the four ‘Milbanke Sound Cones’ (Souther, 1992) that lie along a line projected by

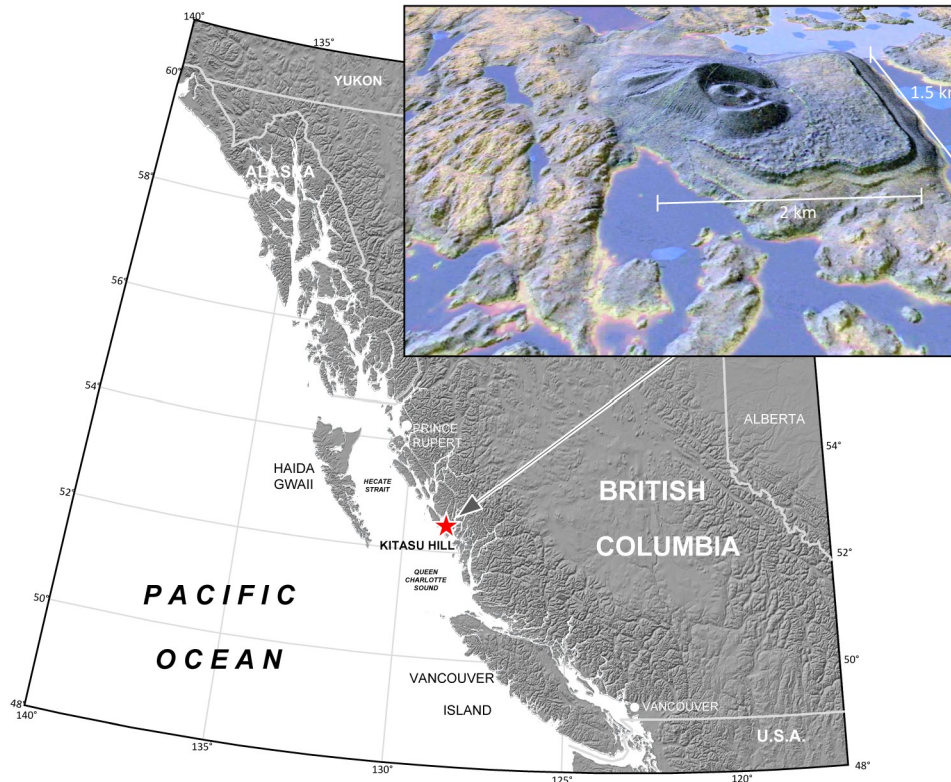


**Figure 1.** Location of the Kitasu Hill volcano on the coast of British Columbia. The feature is composed of a volcanic cone, with a summit elevation of 233 m, overlying a basaltic terrace. The inset is a perspective view, looking north, of a bare earth DEM derived from lidar and coloured as a multi-scale topographic position colour composite (cf. Lindsay, et al., 2015). The higher elevation, well-preserved volcanic constructional features in grey contrast with the lower elevation, glacially scoured bedrock.

investigation of Kitasu Hill, part of an ongoing study of the neotectonics of coastal British Columbia. Although extinct, this volcanic cone is well-preserved and previous geological observations suggest that eruptions took place in postglacial time (Baer, 1973). Kitasu volcano sits on a northwest-trending topographic lineament that

the Principe-Laredo Shear. There is no evidence of younger or ongoing volcanic activity along this shear zone, but recent ocean bottom surveys by the Geological Survey of Canada (GSC) showed disturbed Holocene sediments, a possible landslide, at the eastern end of Laredo Channel, 18 km northwest of Kitasu Hill.



## Objectives

Research questions arose in 2016 after the GSC contracted Light Detection and Ranging (lidar) and marine bottom surveys covering parts of BC's north coast during ongoing studies of neotectonics and geologic hazards. The Lidar survey produced a one metre bare earth DEM covering 309 km<sup>2</sup> of the south shore Swindle Island and adjacent Price Island. With the forest cover removed, Kitasu Hill was shown to be a remarkably well- preserved volcanic edifice composed of nested cones resting upon a distinct terrace. Subbottom imaging of eastern Laredo Channel showed a disturbed surface, possibly from a submarine landslide.

The volcanic eruption of Kitasu Hill is relevant to the neotectonics of coastal British Columbia because of its apparently young geologic age and location along mapped fault zones, as will be discussed below. The principal aim of the site investigation to Kitasu Hill was to determine the age relationship between its volcanic eruptions and adjoining glacial and/or postglacial sediments. Secondly, was to determine the genesis of the prominent terrace beneath the cones. Thirdly, was to see if there was any association between the eruptions and mapped fault zones. Finally, there was a need to assess any correlation between the disruption of bottom sediment in Laredo Strait and eruptions of Kitasu Hill or Neogene to recent renewed fault motion.

## Physiographic Setting

Kitasu Hill lies within the so-called Milbanke Strandflat, a flat low coastal plain abruptly bordering the mountain and fiord terrain to the east (Holland, 1964, Mathews 1976). The strandflat appears to be a Tertiary erosional surface that truncates rocks of diverse ages and compositions (Baer, 1973; Slaymaker and Kovanen, 2016). It is usually poorly drained with expanses of muskeg and bare rock. The rock areas display many distinct lineaments, some running for kilometres. Lineaments mapped in the study area and will be further described in a later section. The genesis of the strandflat is poorly understood because it lies mostly below 30 m in elevation and is very

horizontal, despite cutting across rock of different ages and lithologies, in contrast to the rugged fiord landscape immediately to the east. Nevertheless, subglacial erosion must have been a significant factor because exposed bedrock surfaces show features of intense glacial scour. Such indicators reveal a divergence in glacier flow near Kitasu Hill that will be discussed later.

## Geological Setting

Post accretionary intrusive rocks of the western Coast Plutonic Complex underlie most of the mid coast of British Columbia along an 80 km wide belt. Generally, the plutons young inland from the Late Jurassic to Eocene (based on U-Pb ages; Gehrels et al., 2009) and date from the Early Cretaceous in the study area. Alexander terrane, a large composite crustal fragment of Paleozoic deformed and metamorphosed stratified rocks (Wheeler et al., 1991), is exposed as narrow pendants between the coastal plutons. On Swindle Island and surroundings, Alexander terrane is predominantly Devonian clastic-carbonate strata (Fig. 2; Mathieson Channel Formation; Nelson et al., 2010, 2014).

Major faults transect the area. The southern projection of the Grenville Channel fault passes through Klemtu Pass at Klemtu on Swindle Island, crosses Finlayson Channel, and continues south through Jackson and Oscar passages and into southern Mathieson Channel. Grenville Channel fault is an upper crustal mid-Cretaceous sinistral fault with nearly pure transcurrent motion of regional extent (>150 km), however, some older Early Cretaceous, deep crustal, distributed sinistral-oblique shearing is also evident (Nelson et al., 2010). If both the Grenville Channel and Laredo faults were active at the same time, a NW-SE compression as well as a NE-SW extension would have been the setting for the Lake Island volcanics.

Brittle reactivation of many faults occurred in the Neogene as the Queen Charlotte basin

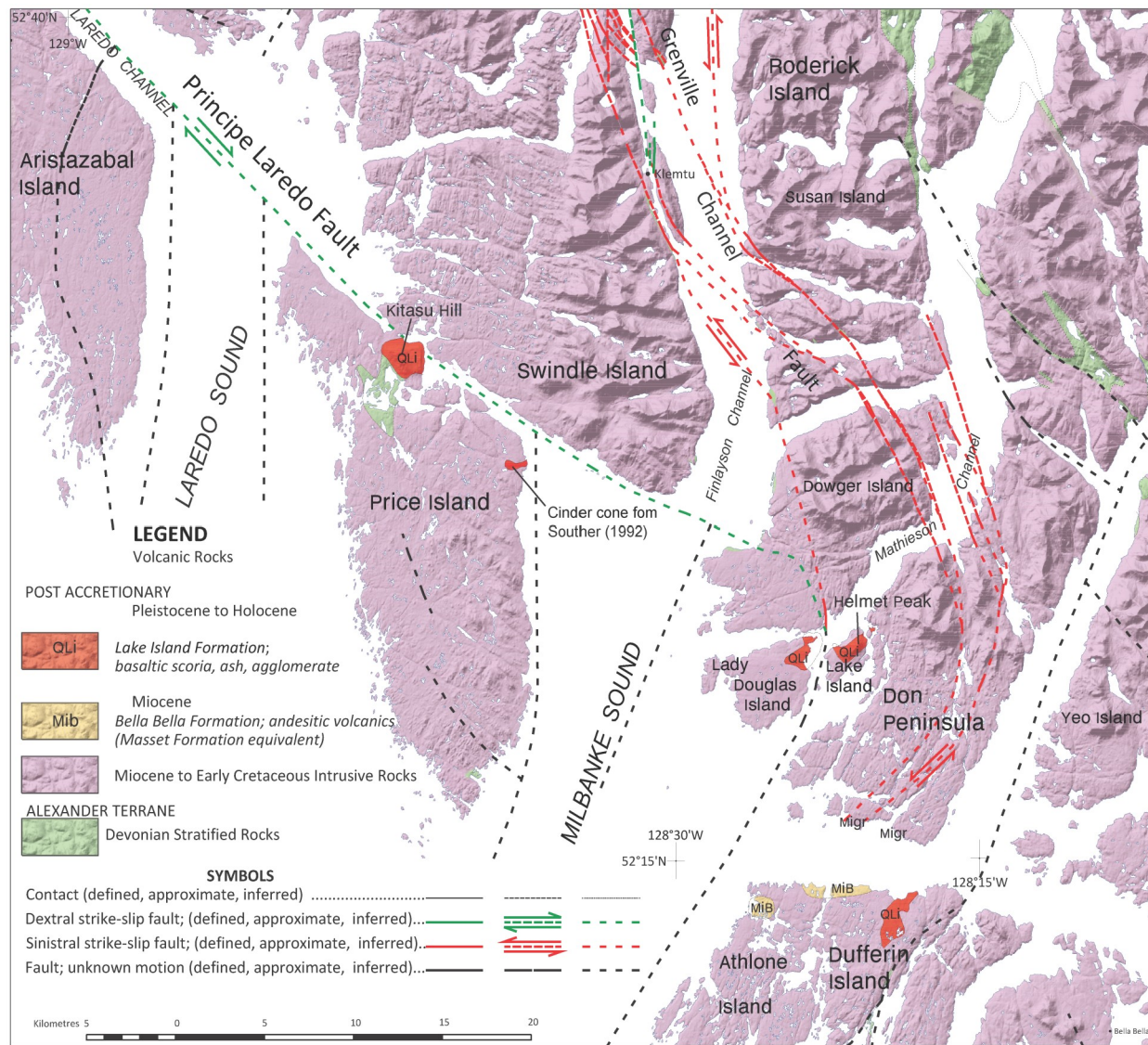


**Figure 2.** Simplified bedrock geology map of the study area with emphasis on the Lake Island Formation (derived from Nelson et al., 2010, 2014). Note the addition of the fourth Milbanke volcanic cone on Price Island (based on the lidar DEM and Souther, 1992).

developed. Magnetic signatures suggest that Milbanke and Laredo sounds are underlain by grabens that probably developed because the southern end of Principe-Laredo shear zone hooks around Lady Douglas Island and cannot be traced further south onto the Don Peninsula, indicating a detachment in which the extensional structures to the southwest are accommodating the motion (Fig. 2; Rohr and Dietrich, 1992; J. Nelson, 2017, pers. comm.). Consequently, the Principe-Laredo fault zone, on which Kitasu Hill sits, is part of a transtensional system defining Milbanke and

Laredo sounds that shows dextral and extensional faulting defining a basin about 5 km deep that extended across the whole of Queen Charlotte Basin (Rohr and Dietrich, 1992; Nelson et al., 2014). Although the Principe-Laredo shear zone showed large scale deflections indicating sinistral kinematics (Chardon et al., 1999), local rocks along the sides of the waterways are brecciated by late faulting with slickensides indicating dextral offsets (Roddick, 1970; Baer, 1973). Northwest of the study area, the Principe-Laredo fault is

shows approximately 80 km of dextral offset, based on displacement of the northern end of the Banks Island plutonic suite (Nelson et al., 2014). Nonetheless, Baer (1973) noted that the dextral offset of a pluton on southeast Aristazabal Island did not exceed 5 km. This is similar to the setting for many of the older Tertiary Masset Formation grabens beneath Hecate Strait and Queen Charlotte Sound.

The topography of the area further suggests a dextral motion on the Principe-Laredo fault. For example, the north-to-south coastal alignment of Laredo Sound and Laredo Inlet indicates about 6 km of right lateral displacement, suggesting a relatively young, possibly Neogene age (Fig.2). Moreover, based on offshore seismic reflection northwest of Banks Island Rohr and Dietrich (1992) suggested that the northern extension of the Principe-Laredo fault under Hecate Strait forms the

southwestern boundary of a half graben with a minimum vertical offset of about 3 km. Based on the thickness of Tertiary sediments against the fault, Rohr and Dietrich (1992) show that the location and preservation of volcanics is controlled by half grabens and flower structures throughout the region. There was a partitioning of slip along the fault in space and/or time so that superimposition of a Miocene transtensive phase was followed by a transpressive phase in the Pliocene, as determined from stratigraphic volumes (Hydman and Hamilton, 1991) and from sea floor stripes (Engebretson, et al., 1985).

Other surface faults and fractures in the Kitasu Hill study area were determined from various topographic lineaments mapped from the lidar DEM (Fig. 3) and discussed in a later section.

## Milbanke Sound Cones – Lake Island Formation

Dolmage (1922) first described four small areas of volcanic flows and tuffs around Milbanke Sound, which he mapped as the “Lady Island formation”. He thought these eruptions were recent in age, likely post glacial, because the deposits rested on glaciated surfaces. Subsequently, these outcrops were renamed the Lake Island formation by Baer (1973). Baer (1973) described the Lake Island formation as composed of brown, red or black unconsolidated ashes, agglomerates, scoriae and subordinate flows. Lake Island basalt is characterized by abundant 0.5 to 1 cm phenocrysts of labradorite and clinopyroxene.

The four areas originally mapped by Dolmage (1922) were described as the monogenetic “Milbanke Sound cones” by Souther (1992). Of the four cones, Kitasu Hill has the best preserved edifice. Helmet Peak on Lake Island, 30 km to the southeast also retains some of its original form, but the other two cones on Price and Dufferin islands are described as eroded mounds (Fig.2).

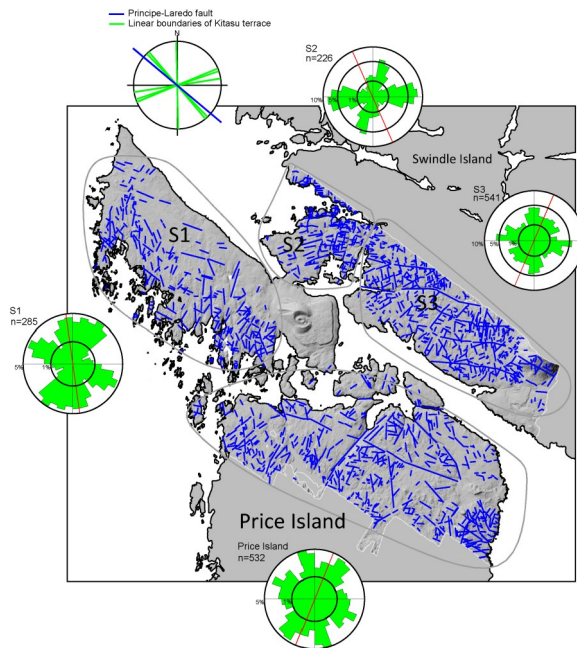


**Figure 3.** Major bedrock lineaments in the study area mapped from the total extent of the lidar DEM. The rose diagrams summarize four areas around Kitasu Hill, as well as, the orientations of the rectilinear edges of the Kitasu terrace (see Fig. 4) and trend of the Principe-Laredo fault.

It should be noted that, of the four Milbanke Sound cones, the cone on eastern Price Island does not appear on Baer's geology map. This is likely a cartographic error as Baer (1973) described basaltic columnar flows on the east shore of Price Island situated 3 km south of the mouth of Higgins Passage. These flows are about 6 metres thick, dipping 20 degrees towards the sea (implying a post eruption tilt) and appear to be the same outcrops originally mapped by Dolmage (1922). Moreover, Souther (1992) clearly shows the location of the Price Island cone on a small inset map. The outcrops on Price Island are not mapped on the most recent geology maps recompiled for the area (e.g. Nelson et al., 2014). However, the Price Island cone is tentatively mapped in Figure 2, based on resistant mounds expressed in the lidar DEM described below.

The Milbanke Sound cones are geographically spaced over ~43 km, following along the Principe-Laredo fault as it trends south-eastward from Kitasu Hill to Helmet Peak. As the fault approaches Helmet Peak, it curves southward and converges with the Grenville Channel fault zone (Fig. 2; Nelson, 2011b). Of the two eroded cones, the one on the eastern shore of Price Island, lies about 3 km south of the mapped Principe-Laredo fault, while the one on the north shore of Dufferin Island is situated on the converged south-trending Grenville Channel and Principe-Laredo fault zones. Dolmage (1922) noted that all extrusions on Lady and Lake islands lie close to a line striking north 50 degrees west, which coincides the Principe-Laredo/Grenville Channel fault zones. These faults likely reactivated and acted as conduits for the basaltic magmas.

As noted, Dolmage (1922) thought that the Lake Island eruptions were postglacial in age because the flows rested on glacially striated granodiorite and quartz diorite surfaces. Furthermore, Souther (1992) reported that parts of Lake Island and adjacent Lady Douglas Island are covered by moderately welded basaltic tuff breccia resting on either glaciated granitic rock or locally on "unconsolidated beach gravel". Likewise, the

eroded remnants on Price and Dufferin islands were reported to have basaltic flows resting over beach deposits on adjacent shorelines (Souther, 1992). Evidence of postglacial eruptions was also observed at Kitasu Hill where ash was found to rest on a glacial till that, in turn, overlaid plutonic rocks. However, lithologically similar pebbles found within the till suggest that some of the eruptions took place during glacial times (Baer, 1973). Moreover, on Lake Island, Baer (1973) noted that basaltic dykes, lithologically similar to the volcanic flows, cut the quartz diorite basement along a north-south axis. Because the dykes have been glacially striated before the agglomerate was deposited, some volcanic activity must have taken place before final deglaciation. Consequently, it appears that the eruptions spanned the late-glacial to postglacial period. Moreover, given that some of these eruptions occurred during glacial times, it is proposed here that the varied state of preservation of the four Milbanke cones may be related to local variations in the intensity of erosion during the final stages of the Fraser Glaciation.

## Geomorphology

### *Lidar DEM*

Geomorphological analysis of the Kitasu edifice was made possible by a lidar survey that effectively penetrated the vegetation to revealed the fine topographic details. The survey was done on May, 2016 using a Riegl 580 (1060 nm) laser scanner and an Applanix POS AV Inertial Measurement unit (IMU/GNSS). The flight trajectory of the aircraft was determined using a combination of permanent GPS/GNSS ground stations and Applanix post processing software that yielded vertical and horizontal positional uncertainties better than  $\pm 15$  cm ( $1\sigma$ ). Average point density for the lidar surveys was 11.58 per m<sup>2</sup> with an effective sampling diameter of 10-20 cm. The lidar point cloud data was classified into ground and non-ground returns using LAStools software. The ground points were triangulated into a TIN and subsequently rastered into a bare earth DEM.



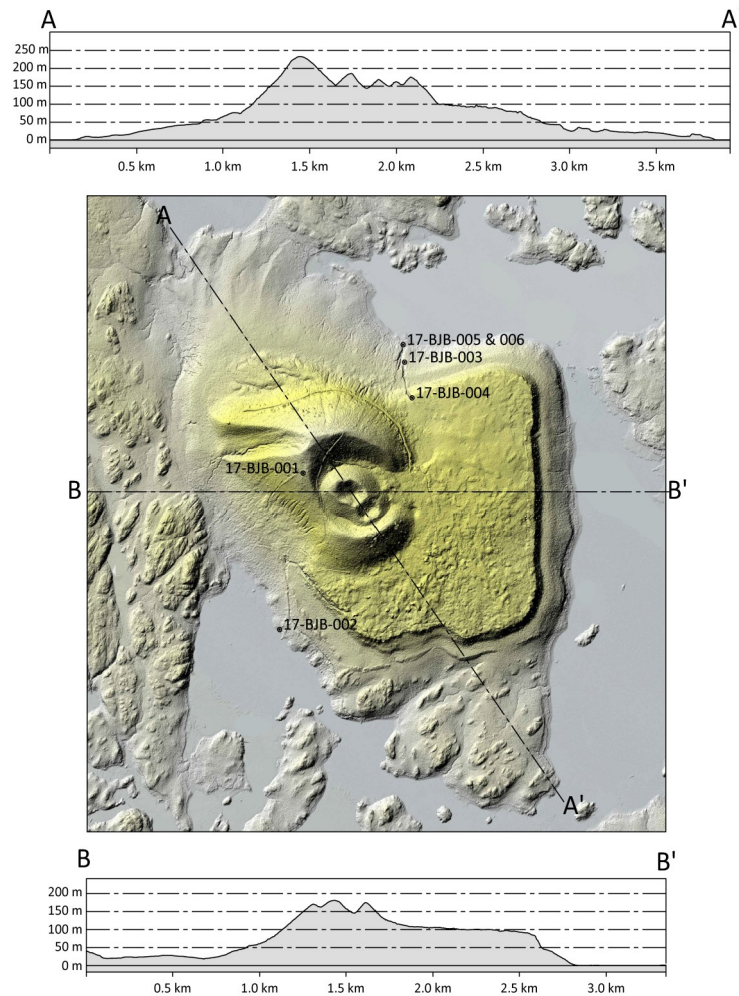


**Figure 4.** Lidar Dem of edifice with topographic cross sections (vertical exaggeration x2). The summit of the largest cinder cone reaches 233 m asl. Also note the basaltic terrace terminating at about 80-85 m asl and the remarkably level lower platform terminating at 42 m asl. Two prominent gullies are cut along the north west side of the terrace. The cinder cones overlie the terrace and mass wasting debris off the main cone partially covers the lower platform on the north side of the terrace. Other landslides of various ages are found on the southwest-facing flank of the cinder cone. Sample locations as indicated.

Owing to the dense forest cover on Kitasu Hill the ground point coverage averages 3 per m<sup>2</sup>. For this study, raw the lidar point cloud data of selected areas was further processed with Whitebox GAT software in order to improve the quality bare earth DEM. Multibeam bathymetry was conducted by the Canadian Hydrographic Service surveys 2009-2013, utilizing a Kongsberg-Simrad EM 710 system operating at 70–100 kHz for water depths greater than 50 m, and an EM 3002 system for

inshore areas of >5 m depth. The output data were gridded to a resolution of 5 m.

#### *Salient features*

Kitasu Hill stands out abruptly, being surrounded by lowlands and the sea. The bare earth DEM reveals a large cinder cone with over 200 m of relief. Kitasu Hill has the morphology of an asymmetric subaerial cone. The northwest elongation and narrower cone to

the southeast near the breach imply a prevailing wind from the east-southeast.

A central crater harbours two successively smaller cones, also with central depressions within (Fig. 4). The cones have steep slopes (25-30°). The rim of the main cone is sharp-crested but it has been breached on the eastern flank so that it has a crescent shape in plan view. The highest point on the main cone is 233 m above sea level (asl), whereas the intermediate cone reaches 190 m in elevation. The smallest cone occupies the south-eastern flank of the intermediate cone. Several small circular depressions resembling collapse features are found within inner cones as well as just outside the south crescent tip of the main cone. They are 30-40 m in diameter and less than 10 m deep.

The base of the main cone overlies a prominent platform on its southern and eastern flank. In plan-view the platform has a sharp outline forming an approximately straight-sided polygon (orientations plotted in Fig. 3). The morphology is terrace-like with a relatively smooth upper surface sloping gently from ~100 m asl, near the foot of the cone, to ~80 m asl at its outer edge over a distance of 700-800 m (~1.5°). The edge of the terrace is abrupt. Contours of the upper terrace surface define a subtle fan shape with the apex coinciding with the breached flank of the edifice (Fig. 4). As will be described below, the terrace appears to be comprised entirely of basalt, moreover, the morphology of the top surface suggests that the terrace covered by lava flows originating from a breach in the main crater (Fig. 5).

In profile, the outer edge of the terrace slope drops abruptly from 80 to 47 m asl (35-40° slope) and then becomes gentle, dropping to 42 m asl over a horizontal distance of about 30 m (~5° slope, similar to beaches). Below 42 m, the slope steepens again to a moderate 15-20°, dropping sea level (Fig. 4). This characteristic break in slope encircles the terrace for over 5 km resulting in a remarkably horizontal bench that appears to cut into the side of the terrace. Nevertheless, current

evidence can not determine whether this feature is erosional or depositional. Along the southern margin of the terrace, the 42 m asl bench seems to intersect a small, discontinuous basaltic ridge that is not horizontal, but drops in elevation to the east and west. In contrast, where the Kitasu cone overlies the terrace, the northern part of the horizontal bench can be traced onto the

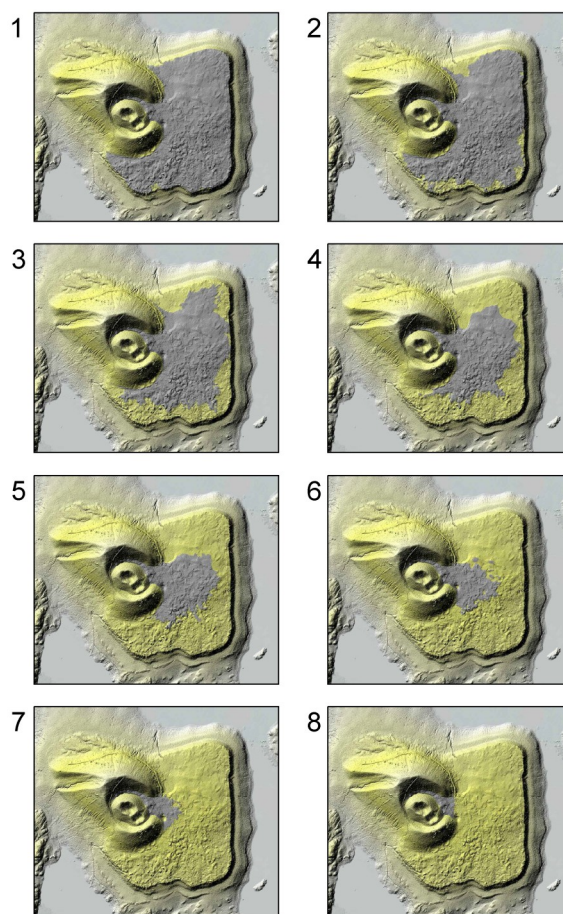


**Figure 5.** A hypothetical sequence of lava flows issuing from the breached Kitasu cone and onto the terrace surface. Based on observations from modern eruptions, the initial, more extensive flows were followed by less extensive, subsequent flows that built up the lava pile progressively towards the vent. The high resolution contours derived from the bare earth DEM delineate individual lobes of lava in the sequence.

flanks of the cone, but with more subdued

breaks in slope. The DEM shows that the slopes may have been smoothed by partial burial with mass wasting debris off the steep gullied slopes of the main cinder cone (Fig. 4). The southwest-facing slope of the cone also has scars of larger landslides of various ages. There is also a small part of the Kitasu terrace on its northern side that was not covered by the cinder cone. The exposed part of the terrace is incised by two narrow gullies that run obliquely across the slope, descending eastward. The 4 m deep gullies start abruptly at about 80 m asl and terminate at about 47 m asl, just above the 42 m asl bench that encircles the terrace.

The relative age of the various landform elements comprising Kitasu Hill can be estimated based on

their morphostratigraphic order. The basalt terrace underlies the volcano and is the oldest landform. The next oldest features are the oblique gullies that were eroded into the north flank of the terrace. The horizontal bench encircling the terrace at 42 m asl is likely next in relative age because the gullies end above the bench. In turn, the bench is likely older than the main pyroclastic cone because it is partially covered by debris that washed off flanks of the main cone. Moreover, the cinder cone appears to overlie the entire northwest quadrant of the terrace. At some point in time the main cone was breached with lava eroding the thinner southeast crater wall and spilling out of the main crater onto the terrace (Fig.5). This must

**Table 1.** Kitasu Hill morphometry

	Total edifice	Main cone	Inner cone 1	Inner cone 2	Terrace	Total
Basal Area (km <sup>2</sup> ) (plan view)	—	0.896	0.071	0.024	3.691	—
Basal width <sup>a</sup> (km)	—	1.068	0.301	0.174	2.168	—
Height (m)	—	148	37	40	100	233
Volume (km <sup>3</sup> )	0.04392	0.04208	0.00153	0.00031	0.18652	0.23044
Rim area (km <sup>2</sup> )	—	0.247	0.021	0.011	—	—
Rim width <sup>a</sup> (km)	—	0.561	0.164	0.118	—	—
Height/basal width	—	0.14	0.12	0.23	—	—
Rim width/basal width	—	0.53	0.54	0.68	—	—
Ellipticity index <sup>b</sup>	1.8	2.2	2.2	—	1.6	—
Irregularity index <sup>c</sup>	1.3	1.2	1.8	—	1.4	—
Long axis azimuth (°)	124	166	107	—	128	—
Average slope (°)		24	25	22	11	—
Elevation range		44-233	128-191	133-174	1-115	—

<sup>a</sup> basal and rim widths are the circle diameter with equivalent area as the basal area

<sup>b</sup> the elongation of the basal footprint and elevation contours the enclose the edifice (averaged)

<sup>c</sup> the measure of flank roughness (area of enclosing contour compared to its perimeter, corrected for ellipticity and averaged every ~20 m in elevation)



have taken place before the final minor eruptions that formed the two small cones within the main crater. The cinder cones are obviously subaerial features but the underlying basaltic platform has a peculiar shape and composition suggesting subglacial deposition. This will be addressed in a later section.

### *Morphometry*

The lidar DEM provides basic morphometric parameters for the edifice were derived with methods described by Grosse et al. (2012). Such parameters are commonly used in global databases (e.g. Grosse et al., 2014). The global databases only describe larger volcanoes (basal width > 2km) limiting comparisons to Kitasu Hill, nonetheless measurements are comparable to morphometric descriptions of monogenetic, subaerial cinder cones in other parts of the world (e.g. Wood, 1980a and 1980b, Inbar et al., 2011).

The surface extent of the cone (footprint) was delineated by a distinct break in slope from surrounding flat-lying terrain (Fig. 4). For this study, the outline of the footprint was used to infer a basal surface underlying the edifice. The basal surface was derived from a triangular irregular network surface (TIN) computed from the basal outline using vertex elevations from the lidar DEM. This surface was then used as the basement to calculate the height and volume of the edifice. Of course, this method only approximates the hypothetical land surface prior to the eruption and cannot represent the entire volume of erupted material. The height of the cone is defined as the summit elevation minus the basal surface elevation directly below the summit. For Kitasu Hill, volumes were calculated for the main and inner cones together and separately, as well as, for the cones and underlying terrace. The terrace basal footprint and surface area was determined with the same method as the cones.

Table 1 lists the principal morphometric parameters describing the cones following the methods described in Grosse et al. (2012). The volume calculations were made with the 3D

surfaces, whereas the shape parameters were calculated using the plan views of the footprints and various enclosing elevation contours shown in Figure. 4.

### **Ground survey**

The study area was accessed by boat through Higgins Passage. Kitasu Hill is thickly forested down to the tide line making ground traverses difficult and exposures limited. Detailed descriptions of the rock and diamicton samples are found in Appendices 1 and 2 with locations in Fig. 4. In general, all the rock samples are alkaline basalt with a nearly identical rock chemistry.

On Kitasu Hill itself, heavily wooded second growth forest and thick undercover makes ground observations especially difficult. However, a few windblown trees on the edifice exposed a substrate composed of tephra, scoria cobbles and blocky basaltic fragments, the likely composition of the entire pyroclastic cone. Figure 6 shows a slightly oxidized scoria bomb found beneath a tree throw (sample 17-BJB-001).

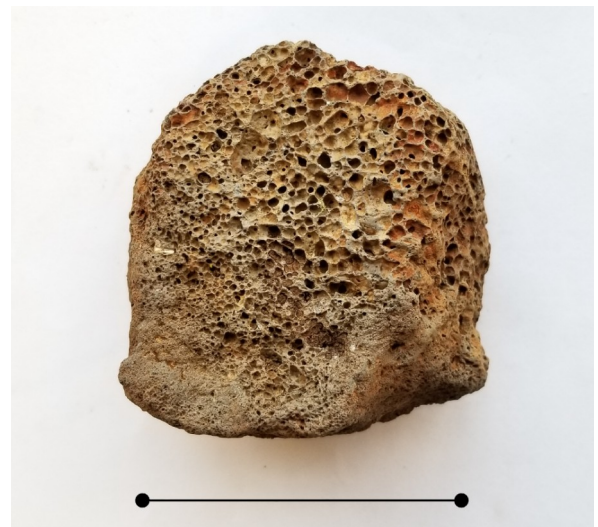


**Figure 6.** A scoria bomb taken from the western flank of the main cinder cone near the summit. Bar is eight cm long.



**Figure 7.** a) Dark basalt platform exposed below the high tide line along the southwest shore of Kitasu Hill. b) Clean exposures of the surface show the flat-lying basalt with pahoehoe flow features. The image spans about 1 m across.

The basement bedrock underlying Kitasu Hill was not evident during the ground survey. Nonetheless, dark, flat-lying basalt lies just below the high tide along the southwest shore at the foot of Kitasu Hill (Fig. 7a). This basalt may form a platform that underlies part of the volcanic edifice, which is immediately east of it. Unweathered surfaces of the platform display flow structures resembling pahoehoe (Fig. 7b). An associated sample (17-BJB-002) was obtained nearby from freshly broken fragments of dense basalt, apparently used to construct a jetty some decades ago. One side of the angular fragment showed subtle flow bands about

1 cm thick. Later inspection showed that the sample was slightly vesicular when cut open and a thin section showed abundant flow aligned phenocrysts (Appendix 1).

As indicated by the lidar DEM, the prominent terrace appears to abut and/or underlie the Kitasu cones. The composition of the terrace was discovered in only a few gully cuts on the north side of the terrace (Fig. 4). The main gully was cut by a northward-flowing stream originating in the crater, but significant incision only starts near the lip of the terrace at about 76 m asl and continues down to about 3 m asl with 3-8 m in relief (Fig. 4). In general, all the

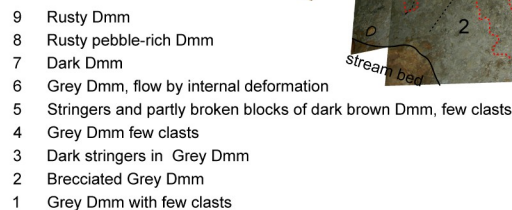


**Figure 8.** A gully incision through the north side of the Kitasu terrace exposing basaltic pillows of breccia basalt. Site of sample 17-BJB-004.

exposures, including the stream bed, show fragments of pillow breccia (Fig. 8). Two oriented rock samples were extracted from the gully: one extracted from the lower part of the terrace at 24 m asl, near the stream bed (Fig. 4; 17-BJB-003) and a second, about 200 m upstream, near the top of the terrace at approximately 68 m asl, from the gully face (Figs. 4, 8; 17-BJB-004). The results of the paleomagnetic analysis is provided in Appendix



003) is slightly less oxidized (<0.2 mm brown rind) with fewer vesicles (~5%) than the upper sample (17-BJB-004; 6 mm brown rind and 12-



In thin section, both samples are show dense grey basalt with about 20-30% of glassy groundmass, flow alignment, a few granodiorite xenoliths, and evidence of rapid hydration and quenching (see Appendix 1). However, the lower sample (17-BJB-

In general, pillow breccias require slopes  $>5^\circ$  with cooler lava or higher quench rates otherwise sheet flows develop (Gregg and Fink,

1995). The basaltic flows exposed within the gully likely make up most of the terrace platform.

Nevertheless, near the mouth of the stream at about 6 m asl, a small cut bank exposes diamicton layers with a total thickness of 2-3 m (Fig. 9). Stratigraphically, the diamicton layers appear to underlie the pillow breccias comprising the main terrace, although this section is ~30 m downstream of the nearest basalt outcrop (samples 17-BJB-005 and 006; Fig. 4). In general, there are two diamictons that are most distinct: a lower a light grey diamicton (10Y8/1) with subrounded to subangular clasts suspended in a very fine sand matrix, overlain by a darker diamicton with a matrix of poorly sorted, very-coarse to fine sand-sized grains with many rounded to angular lithic fragments. Parts of the diamicton are rusty coloured (7.5YR6/6). Near the top of the section the darker diamicton becomes interbedded with wedges of indurated rusty-orange gravel and gravelly diamicton. Although both of the diamicton units are very indurated, the upper diamicton is more indurated and has more clasts. Both units also have larger plutonic clasts, up to 15 cm long, and many are faceted and bullet-shaped, as is typical of glacially transported erratics. Clast compositions are mostly Coast Mountain plutonic material confirming some glacial transport. Layering within the diamictons is evident by composition and colour with apparent shear planes and fold structures. The lower grey diamicton, in particular, has bands of darker material forming stringers of deformed sediment. In general, the unit and erosional boundaries gently dip down to the north and elongated clasts exposed on the face of the section also have a preferred orientation along a north-south axis. It is evident that the diamicton layers accumulated under some traction. In some places the diamictons have clast fabrics typical of a basal till whereas other places internal deformation suggests re-sedimentation of glacial deposits and mixing with local volcanic material with flow structures and soft sediment deformation in a water saturated environment (Fig. 9).

Based on the field descriptions, the diamictons were initially interpreted as a mixture of glacial deposits and volcanic material in a subaqueous environment. At first approximation, this interpretation agrees with earlier geological reports that described the Kitasu Hill lava flows as overlying glacial till (Baer, 1973). However, sample thin sections show that the diamictons are composed mostly of locally derived olivine basalt dominated by glassy shards and largely a product of quench fragmentation (volcanic rock fragments, palagonite and brown glass). Moreover, the volcanic material could not have travelled far from the vent because of the well-preserved state of abundant fragile glass and chemically unstable glass and olivine. Consequently, the diamictons are interpreted as hyaloclastites and/or resedimented hyaloclastite (Appendix 1). Nevertheless, these hyaloclastites contain an abundance of admixed plutonic minerals and glacial erratics of Coast Mountain plutonic provenance (sample 17-BJB-005 is ~ 20% plutonic rock fragments and minerals) that require an explanation. The contemporaneous deposition of these disparate materials can be explained by two possible mechanisms. Possibly, the magma migrated to the surface it may have disrupted a surface layer of glacial till. However, till cover in this region is very thin and discontinuous, suggesting that the amount of glacial material available for mixing would be minimal. Alternatively, if the volcanic eruption took place under a debris laden ice sheet, magmatic heat could melt a cavity into the base of the glacier and, in such a case, meltout of englacial debris would rain down upon the erupting material and cement it hydrothermally as it was deposited. The latter explanation is considered the most plausible for the Kitasu eruption.

## **Tuya hypothesis**

As described above, hyaloclastite underlies the volcanic terrace that shows that a significant volume of water was present during deposition. Moreover, a significant portion of the

hyaloclastite contains Coast Mountain plutonic rocks and minerals that require some glacial transport to the site. It is proposed that the syndeposition of fresh volcanic debris with the plutonic material can best be explained by a subglacial eruption in a meltwater-filled vault. Furthermore, the initial subglacial effusion probably persisted to build the overlying lava pile that ultimately formed the steep-sided basaltic terrace. Petrographically, the overlying pillow breccia is very similar to the underlying hyaloclastite indicating a single volcanic source (see Appendix 1) and the paleomagnetic data also suggests that the terrace basalts accumulated very quickly (see Appendix 2). Accordingly, it is proposed that the rapid accumulation of the lava pile in a subglacial environment ultimately produced the unique shape to the Kitasu volcanic terrace, meaning that the Kitasu terrace is a *tuya* formed in contact with subglacial water (cf. Mathews, 1947; Hickson, 2000; Russell et al., 2014). Accepting this explanation, the Kitasu Hill edifice is considered to be a composite feature with subsequent eruptions forming the monogenetic cinder cones in a subaerial environment after deglaciation.

Russell et al., (2014) defined tuyas as “*positive-relief volcanoes having a morphology resulting from ice confinement during eruption and comprising a set of lithofacies reflecting direct interaction between magma and ice/melt water*”. Jones (1968) noted that ice-contact volcanoes in Iceland range from steep-edged piles of flat-lying pillow lava to steep-sided table mountain-like tuyas and he proposed a qualitative model for subaqueous volcanoes that describe stages of development culminating in flat-topped tuyas (see Jones, 1968; Hickson, 2000). Briefly, the initial phase begins when a fissure or pipe erupts into the base of an ice sheet and magmatic heat melts a water-filled cavity. Effusion of lava into the meltwater builds a steep-sided pillow lava pile. In time, the lava pile accumulates until the roof of the ice cavity collapses into an englacial lake. If the lava pile continues to accumulate to within ~200 m of the water surface, explosive ejection of vitric

ash occurs with tuff accumulating between the wall of ice and the pillow pile. Eventually entire pillow lava pile is capped by tuff. In some cases the central accumulation emerges from the lake, explosive eruption ceases, and quiet subaerial effusion of lava covers the tuff. However, should the outward flowing lava reach the water's edge it granulates forming flow-foot breccias on the steep fronts, much like foreset beds deposited on a delta front. The breccias then cover the earlier deposits of subaqueous effusion and explosive emergence. In the final stage, further subaerial eruptions cover the breccias with sheet lava making gentle slopes, and the flat-topped tuya form emerges from the retreating ice sheet. In summary, tuyas are the end product of a depositional sequence comprised of a pillow lava pile that is capped by tuff and enveloped with a carapace of gently sloping sheet lava over a pedestal of glassy breccia with steep slopes. The planar and horizontal boundary between the carapace and pedestal was believed to record the water level of the subglacial lake in which the volcano erupted (Jones, 1968).

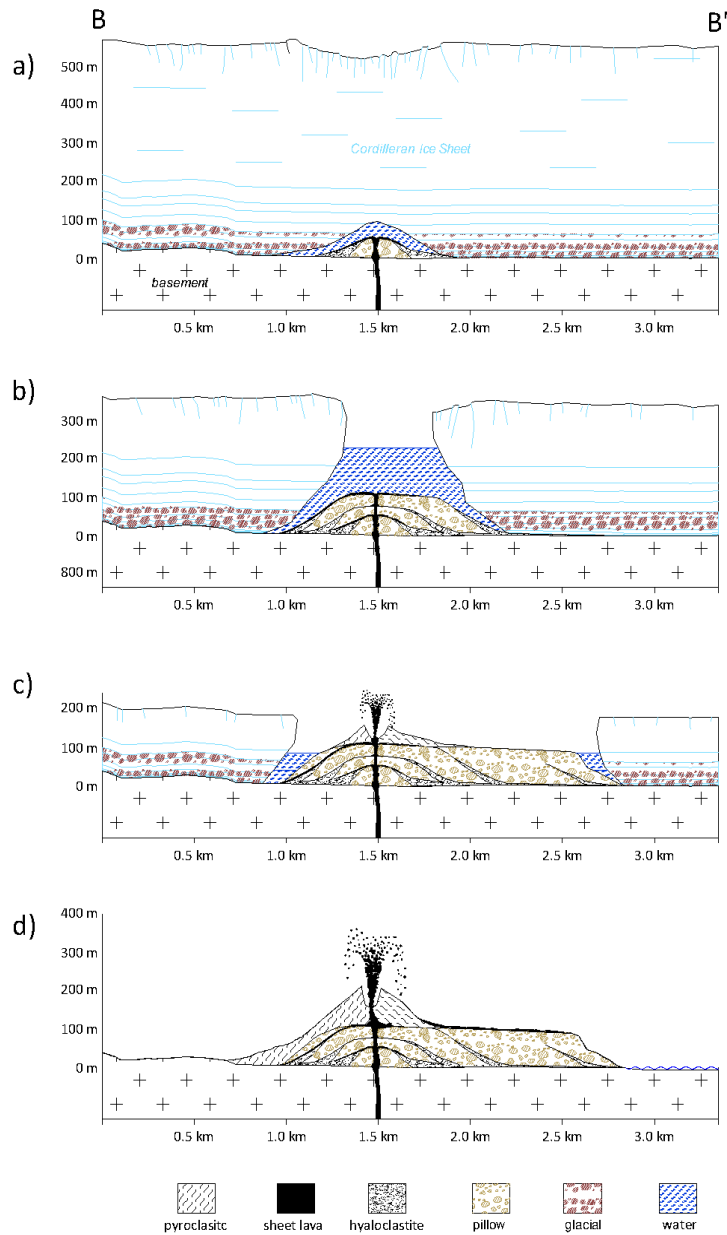


**Figure 10.** The proposed development of the Kitasu volcanic edifice. a) Initial eruption under a significant thickness of the Cordilleran Ice Sheet where magmatic heat melts a water-filled vault into the base of the ice. A lava and hyaloclastite pile builds over the vent as glacial debris melts out from the ceiling and mixes with the erupting effusion forming an increasing thickness of sheet flows, pillow breccia and hyaloclastite. b) As the vault enlarges and/or the ice sheet thins the roof collapses forming a subglacial lake. Effusion into a considerable depth of water builds continues to build the pillow breccia pile. Buildup is somewhat controlled by the shape and depth of the subglacial lake. c) Lake levels fall rapidly during deglaciation and continued lava deposition is controlled at changing water's edge. The eruption becomes explosive once the water shallows and drains. A cinder cone develops over the basalt breccia. d) The current Kitasu edifice stands proud once the ice sheet has receded. Continued eruption blew out the east flank of the cinder cone capping the terrace with successive flows. The final eruptive activity built secondary cinder cones within the main crater (not shown). Vertical exaggeration X2.

The classic Icelandic stratigraphic sequence described by Jones (1968) was not seen at Kitasu Hill, specifically the steeply bedded, delta-like, flow-foot breccias. Nonetheless, there is enough similarity between the flat-topped Kitasu terrace and other tuyas in Iceland and British Columbia to suggest that similar processes may have been at work. Especially given the uniformity of the petrography of the sample rocks described above (Appendix 1 and 3). Moreover, because of the limited number of exposures examined in the study area, it cannot be ruled out that dipping flow-foot breccias do not exist given the highly variable nature of lava facies when in contact with water (see Yamagishi, 1991). Figure 10 is a schematic of tuya formation adapted to Kitasu Hill depicted to

geochronological evidence, Dyke et al. (2003) placed the maximal margin of the ice sheet grounded in Queen Charlotte Sound, approximately 62 km south west of Kitasu Hill. Given this extended position, a hypothetical ice profile, derived from empirical data on present-day ice sheets, suggests that the Cordilleran Ice Sheet was at least 800 m thick in the vicinity of Kitasu Hill (Fig.11). The maximum position was reached by ~14,000 to 14,500 radiocarbon years ago (ka BP), however, because the ice sheet was already west of Kitasu Hill by ~18 ka BP and at least some ice cover persisted until deglaciation of the site by ~12.5 ka BP (Dyke et al. 2003), there is roughly a 7000 year interval during which an eruption to form Kitasu Hill

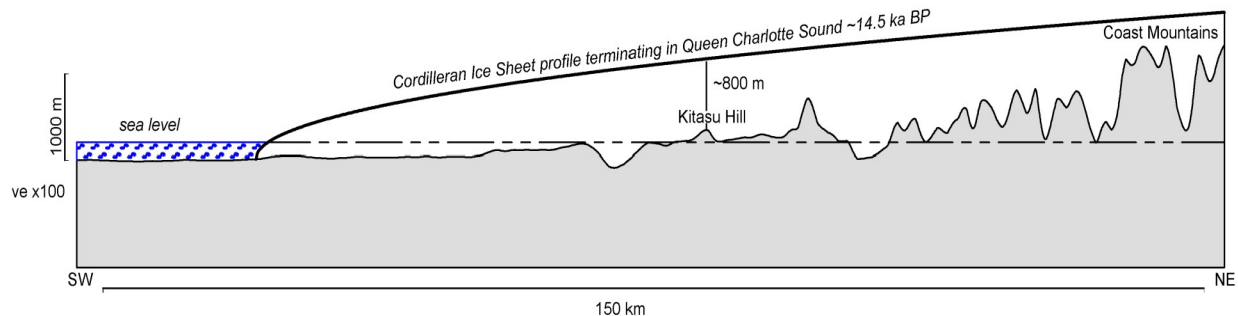


**Figure 11.** A hypothetical ice sheet profile superimposed over a topographic cross-section from the Coast Mountains to its terminus in Queen Charlotte Sound at about 14.5 ka radiocarbon years BP (Dyke et al., 2003). The ice profile is based on empirical data from parts of the Antarctic and Greenland ice sheets (Hollin, 1962; Mathews, 1974) and agree with theoretical glacier profiles determined from the plastic properties of ice (e.g. Ackerly 1989; Schilling and Hollin 1981).

scale. The composite depositional sequence shows the hypothetical buildup of intercalated pillow basalt, sheet lava and hyaloclastite with changing eruptive conditions and changes in the size and depth of the englacial lake. It should be noted here, Kitasu Hill was also subjected to high relative sea levels during the early postglacial period, but sea level did not reach the elevations of the upper terrace, as will be discussed in a later section.

*Glacial conditions in vicinity of the Kitasu volcano*  
During last glacial maximum the Cordilleran Ice Sheet emanated from the Coast Mountains and inundated the outer coast of central British Columbia. Based on geomorphological and

would have been under a substantial thickness of ice significantly impacting the morphology of any volcanic activity (cf. Smellie, 2007).



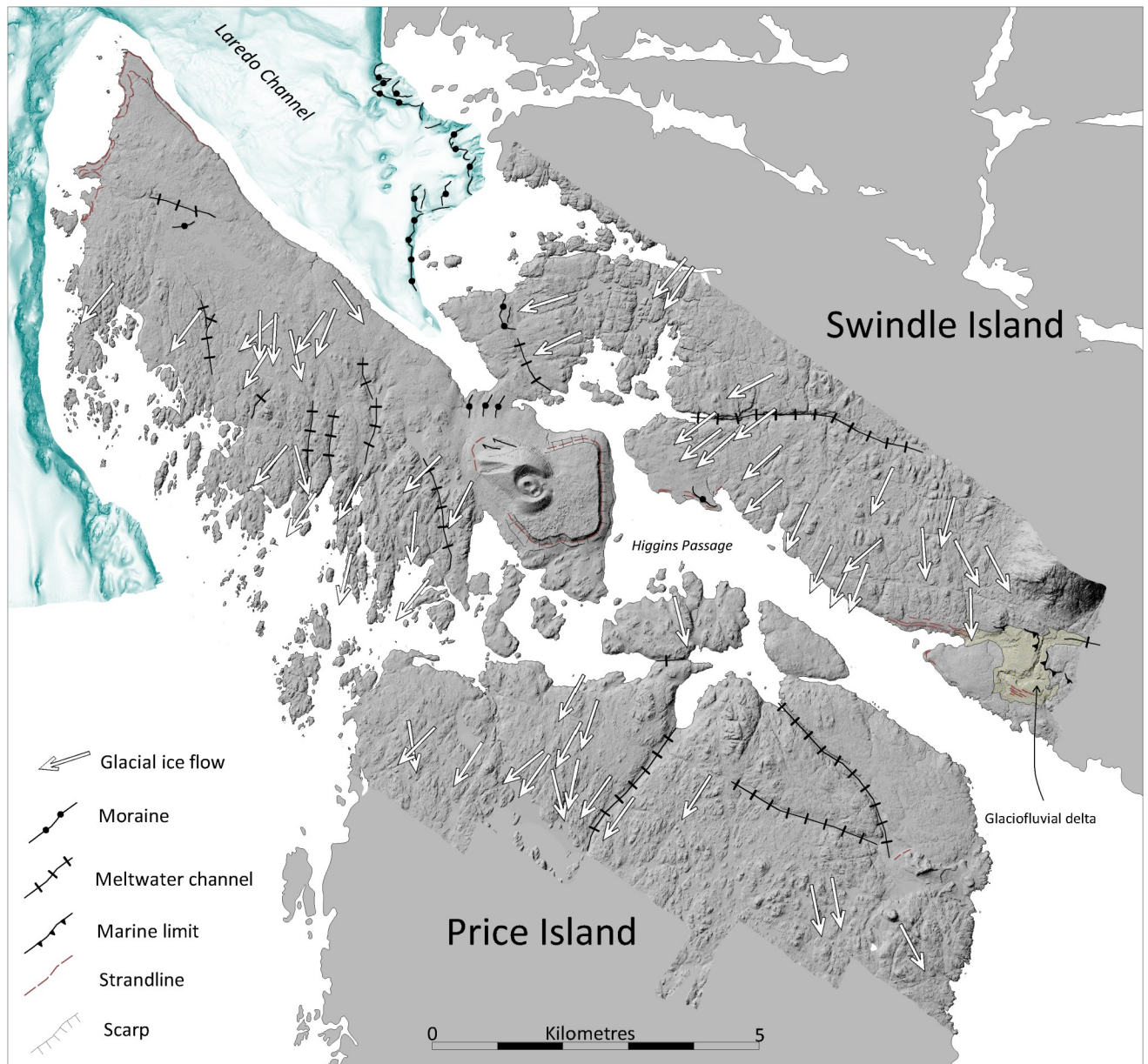


**Figure 12.** Glacial landforms of the study region mapped on the lidar DEM and multibeam bathymetry. Glacially scoured bedrock records the main directions of former ice flows. Cross-cutting patterns reflect changing the changing dynamics of the Cordilleran Ice Sheet, particularly during deglaciation. Meltwater channels formed preferentially along structural troughs. End moraines immediately north of Kitasu Hill mark a retreat position of the ice sheet with terminus bordering the west coast of Swindle Island with small tongues of ice flowing into Laredo Sound. Ice flow was to the west-southwest at this time. Of note are two gullies below the flank of the Kitasu cone that may be lateral meltwater channels cut when the ice margin abutted the north side of the Kitasu terrace. This suggests that the cinder cone may have erupted after the ice retreated from the immediate area. For a short period of time sea level was higher than present during deglaciation. The glaciofluvial delta on the east side of the figure marks a marine limit of ~65 m asl. A horizontal bench encircling the Kitasu terrace must mark a water plane at 42 m asl, however, it is not known where it is from an englacial lake or the postglacial sea level.

The effects of glaciation in the study area are apparent from the glacially scoured landscape with ice-moulded and streamlined bedrock protuberances aligned in the direction of the former ice flow. The main ice-flow elements show a dominant flow direction to the south and southwest (Fig. 12). From the lidar DEM it is clear that many of the streamlined landforms are aligned with the underlying bedrock structure but in some places the ice-flow features also cross-cut the bedrock structure. In other places, sets of ice-flow features cross-cut themselves reflecting shifting flow paths as the ice sheet advanced and subsequently thinned and retreated following the last glacial maximum. An ice flow pattern from the retreat phase is evident north of Kitasu Hill where a westward ice flow dominates. A series of end moraines north of Kitasu Hill and in Laredo Sound lie orthogonal to the retreating ice flow pattern. These moraines formed during minor stillstands in ice retreat (Fig. 12).

The genesis of the two gullies incised across the north flank of the Kitasu terrace are significant for the relative chronology of events at Kitasu Hill. The channels run obliquely downslope and do not have an obvious source area to have been eroded by water. However, if these gullies are lateral meltwater channels, they would mark the position of the ice sheet roughly coeval with the moraine segments along the west side of Swindle Island and eastern Laredo Sound (Fig. 12). This could also mean that the Kitasu terrace might have existed prior to final deglaciation, and hence must be older than ~12.5 ka BP (Dyke et al. 2003).

Although most of the ice flow patterns in the study area mark the advance and retreat of the Cordilleran Ice Sheet, ice-flow features along a ~2 km wide zone bordering the west side of Kitasu Hill swing from southwest to south, an apparent deflection in the vicinity of Kitasu Hill (Fig.12). The present-day topography cannot explain this deflection but perhaps the initial volcanic eruption caused some thermal anomalies at the base of the ice sheet. Nevertheless, this redirection of ice flow must have occurred before the Kitasu volcanic

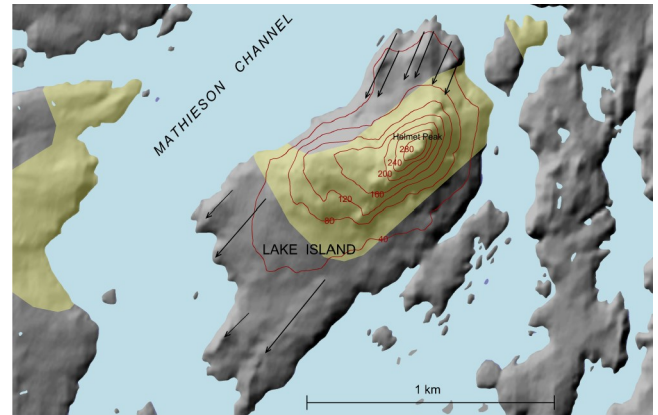


**Figure 13.** *Helmet Peak, Lake Island, one of the four Milbanke volcanic cones, is asymmetrical with the long axis aligned in the direction of former ice flow as indicated by the glacially streamlined bedrock on either side of the cone (flow arrows indicated). This suggests that the cone may have been partially eroded by the ice flowing down Mathieson Channel. The glacial landforms were mapped from aerial photographs. (Lake Island formation, in yellow; from Nelson et al, 2014).*

edifice was constructed because there are no ice-flow features on it. This is in contrast to Helmet Peak, the other well-preserved Milbanke cone that appears to have been partially eroded by a glacier flowing down Mathieson Channel (Figs. 2, 13). It is also probable that the other two Milbanke cones described as mere erosional remnants (Souther, 1992) were nearly completely eroded by glacial action. Glacial erosion can be highly variable depending on ice configuration and location of various ice-flow paths.

## Dating the Kitasu volcanic sequence

If the Kitasu Hill basaltic terrace resulted from a subglacial eruption, its age must be constrained by the interval of ice cover by the Cordilleran Ice Sheet. As previously noted, this would be roughly from ~19-12.5 ka BP in radiocarbon years, based on the chronology of Dyke et al. (2003; also Clague and James, 2002).

Moreover, the existence of the volcanic terrace prior to deglaciation is further confirmed if the channels cutting the north side of the terrace were ice marginal. The age of the volcanic terrace can be further constrained because it was not subsequently overridden by glacial ice after it formed. This suggests that the terrace likely formed during the waning stage of glaciation (~14.5-12.5 ka BP). In addition, it is also more likely that a subglacial lake, in which the lava accumulated, would have formed during glacial recession when ice was thinning and less dynamic.

The main cinder cone built on the Kitasu terrace has a younger relative age, but this can not be resolved based solely on the composition of the erupted rocks. However, the similar petrography of all the samples suggests that only a few weeks or months may have past. Usually cinder cones and cinder cone fields are short lived, monogenetic eruptions from a constrained pulse of lava interacting with the groundwater (Wood, 1980a). The main geomorphic distinction here, is that the cinder cone was a subaerial eruption whereas the terrace accumulated within a subglacial lake. So, either the pyroclastic eruption took place after deglaciation or the eruption took place into a hole in the ice sheet but only after the water level dropped below the top of the terrace. Here, the genesis of the perfectly horizontal bench that encircles the volcanic terrace at 47-42 m asl is significant because it lies at the foot of the cinder cone. As described previously, debris that washed off flanks of the cinder cone partially covers the bench, meaning that the bench is older than the cone. This level bench is interpreted as a strandline that could have formed in the subglacial lake. Accordingly, a subglacial lake would likely date from ~14.5-12.5 ka BP, during the waning phase of Cordilleran ice cover (Clague and James, 2002; Dyke, et al., 2003). In such a case, the absolute age of the pyroclastic eruption cannot be resolved better than the apparent age of volcanic platform. Alternatively, the strandline could also be marine in origin, formed shortly after deglaciation because relative sea level was higher then due to glacioisostatic effects. Moreover, if the strandline

is younger than the lateral meltwater channels cut into the north side of the volcanic terrace above it, it must be marine because once the ice margin retreated to the north side of the Kitasu terrace, meltwater would be free to drain to the south and subglacial lakes could not exist. Consequently, the maximum age of the main cinder cone can be assessed by the age of the 47-42 m postglacial sea level.

There is clear evidence in the Kitasu Hill area that relative sea level was considerably higher than present during early postglacial time. For example glaciofluvial delta terraces ~6 km east of the Kitasu volcano record a marine high stand of at least 65 m asl (Fig. 13). Regionally, postglacial marine high stands recorded at the heads of fiords on the mainland, about 150 km east of Kitasu, are ~150 m asl, even though deglaciation occurred later than at Kitasu Hill. This differential uplift was caused by uneven crustal loading because the former ice sheet was thicker over the mainland than on the outer coast (Andrews and Retherford, 1978). In any event, with deglaciation Kitasu Hill came in contact with a high sea sometime before ~12.5 ka BP (Clague and James, 2002; Dyke, et al., 2003).

The age of the 47-42 m shoreline could be better constrained if the relative sea level history of the study area was known. Letham, et al. (2016) established a relative sea level curve of the Prince Rupert area – a similar setting as the Kitasu site with respect to the retreating Cordilleran Ice Sheet, but ~225 km further up coast. Deglaciation of the vicinity of Prince Rupert occurred sometime before ~15,000 calendar years before present (cal BP; ~12.7 ka radiocarbon years). Relative sea level dropped from ~50 m asl to as low as -6.3 m asl between 14,500-13,500 cal BP, it then rose to at least 6 m asl by ~11,500 cal BP, after which it slowly dropped to about its current position by 2000-1500 cal BP, with some possible fluctuations. Given a similar crustal response to glacial unloading at the Kitasu site, despite the slightly

higher marine limit, the strandline at Kitasu Hill dates from ~14,500 cal BP (~12.3 ka BP). Consequently this is minimum age estimate for the Kitasu volcanic terrace but a maximum age for the Kitasu cinder cone. So the minimum age of the Kitasu volcanic platform derived from the relative sea level history near Prince Rupert (Letham, et al. 2016) is in general agreement with the broad chronology of ice retreat (Clague and James, 2002; Dyke, et al., 2003).

It is reasoned here that whether or not the strandline formed in a glacial lake or the sea, the Kitasu volcanic platform must date from at least the end of the Late Pleistocene. Sometime after the volcanic platform formed, the younger pyroclastic cones erupted unhindered by ice or the sea. The first subaerial eruption occurred after the sea receded below 42 m asl because masswasting debris off the flanks of the main cone accumulated on the 42 m strandline (Fig. 12). No strandlines appear to trim the cone itself and, because relative sea level fell so rapidly during deglaciation, the absolute age to these subsequent eruptions cannot be resolved any further with this method.

The relative youth of the Kitasu cinder cones can broadly be estimated by assessing the level of degradation of the cones since they were deposited. Porter (1972) suggested that there is an equilibrium angle of repose for fresh cinder cones on Mauna Kea, Hawaii. Porter (1972) established that cone height was usually 18% of cone width and crater width was usually 40% of basal width. The Kitasu cones are more subdued than these values (Table 1), as would be expected if a long period of quiescence followed the eruption allowing the slopes to be diminished and height to be degraded by subsidence or erosion. Inbar et al. (2011) studying the development of Holocene cinder cones in the Tolbachik volcanic field in Kamchatka, noted that the most recent cinder cones could be grouped according to the age of eruption. They found that highest slopes and steepest slopes were always associated with the youngest eruptions. The youngest eruptions from the mid 1970's had average slopes of just under

32°, whereas the older group from the last 1500-1700 years had average slope values from ~26-27°. This was similar to earlier findings of Wood (1980a, 1980b) who found a correlation between cone morphometry and degradation as a proxy for age for 910 cinder cones around the world. The average slopes of the Kitasu cones (Table 1; 24-22°) are also less than an 'older' group of cinder cones in Kamchatka measured by Inbar et al. (2011). However, they noted that erosional processes of the Kamchatka Peninsula are more intense compared to other areas of the world, so if erosional processes at Kitasu Hill were as intense as in Kamchatka, then the Kitasu cones are at least a two thousand years old. If erosion is less intense, then the Kitasu cones could be much older (ie. deglacial). As a side note, eruptions of Kitasu volcano are mentioned in Kitasoo First Nation oral history (V. Brown, 2017, pers. comm.)

## Summary and Conclusions

Kitasu Hill, a small volcano on one of the outer islands of coastal British Columbia is one of the four Milbanke Sound cones that are spaced along Principe-Laredo and Grenville Channel fault zones, however the relationship of the volcano to the fault zones is unknown. The Milbanke cones were thought to have erupted sometime in the Holocene, but the evidence presented here suggests that the eruptions were likely older, near the end of the last glaciation. Coincidentally, during Late Pleistocene deglaciation the four cones had the same relative position with respect to the retreating ice sheet and thus may have undergone similar induced crustal unloading during deglaciation. It is proposed that two of the four Milbanke cones, which are erosional remnants, were eroded by the ice sheet, whereas Helmet Peak, the second best preserved cone was only partially eroded by south-flowing ice in Mathieson Channel.

The Kitasu Hill volcano is composed of an elevated platform of brecciated alkali olivine basalt and lava flows (~100 to 80 m asl)

partially overlain by a well-preserved cinder cone reaching 233 m asl. Parts of the Kitasu volcanic platform are underlain by hyaloclastite containing a mix of locally sourced eruptive material and ~20% mineral grains and glacial erratic cobbles from Coast Mountain plutonic sources. The sediment characteristics and overall morphology of the volcanic platform intimates that the initial eruption took place in an englacial setting during the waning stage of the last glaciation between 14.5 and 12.5 ka BP (radiocarbon years ago). The final pyroclastic eruptions took place sometime after 12.3 ka BP, based on the postglacial relative sea level history of the region.

## Acknowledgements

Kitasu Hill lies in the unceded territory of the Kitasoo/Xai'Xais First Nation (Kitasoo Spirit Bear Conservancy) and the field work was done under the auspices of the Kitasoo Band Office. The authors wish to thank Vernon Brown for guiding and student assistants Jacintha Brown, Robbie Duncan, Tina Lobbes and Mercedes Robinson-Neasloss.

Lidar survey was partly supported by the Canada Foundation for Innovation and NSERC grants to Brian Menounos, University of Northern British Columbia.

## References

- Andrews, J.T., and Retherford, R.M., 1978. A reconnaissance survey of late Quaternary sea levels, Bella Bella and Bella Coola region, central British Columbia coast; *Canadian Journal of Earth Sciences*, v. 5, p.341–350.
- Ackerly, S.C., 1989. Reconstructions of mountain glacier profiles, northeastern United States; *Geological Society of America Bulletin*, v.101, p.561–572.
- Baer, A.J., 1973. Bella Coola – Laredo Sound map-areas, British Columbia; *Geological Survey of Canada Memoir* 372, 122 p., 1:250 000 geological maps.
- Chardon D., Andronicos, C.L., and Hollister, L.S., 1999. Large-scale transpressive shear zone patterns and displacements within magmatic arcs: The Coast Plutonic Complex, British Columbia; *Tectonics*, v. 18, no. 2, p. 278–292.
- Clague, J.J., and James T.S., 2002. History and isostatic effects of the last ice sheet in southern British Columbia; *Quaternary Science Reviews*, v. 21, p.71–87.
- Dolmage, V., 1922. Coast and islands of British Columbia between Burke and Douglas Channels; *Geological Survey of Canada Summary Report for 1921*, pt. A, p. 22–49.
- Dyke, A.S., Moore, A., and Robertson, L., 2003. Deglaciation of North America; *Geological Survey of Canada, Open File* 1574.
- Dyke, A.S., 2004, An outline of North American deglaciation with emphasis on central and northern Canada; *in* *Quaternary Glaciations – Extent and Chronology— Part II, Developments in Quaternary Science*, (ed.) Ehlers, J. and Gibbard, P.L.; Elsevier, Amsterdam, v. 2, p. 373–424. doi:10.1016/S1571-0866(04)80209-4
- Engelbreton, D.C., Cox, A., Gurdun, R.G., 1985. Relative motions between oceanic and continental plates in the Pacific basin; *Geological Society of America. Special Paper* 206, 50 p.
- Gregg, T.K.P., Fink, J.H., 1995. Quantification of submarine lava-flow morphology through analog experiments. *Geology*, v. 23(1), p. 73–76.
- Grosse, P., van Wyk de Vries, B., Petrinovic, I.A., Euillades, P.A., and Alvarado, G.E.,



2009. Morphometry and evolution of arc volcanoes; *Geology*, v. 37(7), p. 651–654.
- Grosse P, Euillades P.A., Euillades L.D., and van Wyk de Vries B., 2014. A global database of composite volcano morphometry; *Bulletin of Volcanology*, v. 76(784), 16 p., doi:10.1007/s00445-013-0784-4
- Grosse P., van Wyk de Vries B., Euillades P.A., Kervyn M., and Petrinovic I.A., 2012. Systematic morphometric characterization of volcanic edifices using digital elevation models; *Geomorphology*, v. 136, p.114–131.
- Hamilton T.S. and Dostal, J. 1991. Melting of heterogeneous mantle in a slab window environment: examples from the middle Tertiary Masset basalts, Queen Charlotte Islands, British Columbia. *Canadian Journal of Earth Sciences*, v.38, p. 825–838. doi: 10.1139/cjes-38-5-825
- Hickson C.J., 2000. Physical controls and resulting morphological forms of Quaternary ice-contact volcanoes in western Canada; *Geomorphology*, v. 32, p. 239–261.
- Hollin, J.T., 1962. On the glacial history of Antarctica; *Journal of Glaciology*, v. 4, p. 173–195.
- Hyndman, R.D., Hamilton, T.S., 1991. Cenozoic relative plate motions along the northeastern Pacific margin and their association with Queen Charlotte area tectonics and volcanism; *Geological Survey of Canada, Paper 90- 10*, p. 107- 126.
- Inbar, M., Gilichinsky, M., Melekestsev, I., Melnikov, D., and Zaretskaya, N., 2011. Morphometric and morphological development of Holocene cinder cones: a field and remote sensing study in the Tolbachik volcanic field, Kamchatka; *Journal of Volcanology and Geothermal Research*, v. 201 (1–4), p. 301–311.
- Jones, J.G., 1969. Intraglacial volcanoes of the Laugarvatn region, south-west Iceland, I. *Geological Society of London Quarterly Journal*, v. 124, p. 197–211.
- Letham B., Martindale A., Macdonald R., Guiry E., Jones J., and Ames K.M., 2016. Postglacial relative sea-level history of the Prince Rupert area, British Columbia, Canada; *Quaternary Science Reviews*, v. 153, p.156–191. [doi.org/10.1016/j.quascirev.2016.10.004](https://doi.org/10.1016/j.quascirev.2016.10.004)
- Lindsay, J.B., Cockburn, J.M.H., Russell, H.A.J., 2015. An integral image approach to performing multi-scale topographic position analysis. *Geomorphology*, v. 245, p. 51–61. doi.org/10.1016/j.geomorph.2015.05.025
- Mathews, W.H., 1947. “Tuyas,” flat-topped volcanoes in Northern British Columbia; *American Journal of Science*, v. 245, p. 560–570.
- Mathews, W.H., 1974. Surface profiles of the Laurentide Ice Sheet in its marginal areas; *Journal of Glaciology*, v. 13, p. 37–43.
- Nelson, J.L., Diakow, L.J., Karl, S., Mahoney, J.B., Gehrels G.E., Pecha, M., and van Staal, C., 2011a. Geology of the mid-coast region of BC near Klemtu, parts of 103A/08, A09, A/15 and A/16; *Geological Survey of Canada, Open File 6762*; B.C. Ministry of Energy and Mines, Open-File 2011-3, 1:100 000 scale.
- Nelson, J.L., Diakow, L.J., Karl, S., Mahoney, J.B., Gehrels G.E., Pecha, M., and van Staal, C., 2011b. Geology and mineral potential of the southern Alexander terrane and western Coast Plutonic Complex near Klemtu, northwestern British Columbia; *BC Ministry of Energy*

- and Mines, Geological Fieldwork 2010, p. 73–98.
- Nelson, J.L., Diakow, L.J., Mahoney, J.B., Gehrels, G. E., van Staal, C.R., Karl, S., Pecha, M., and Angen, J.J., 2014. Geology of the north and mid-coast regions, British Columbia (parts of NTS 1 03-A, -G, -H, -I and -J); Geological Survey of Canada, Open File 7604; British Columbia Geological Survey Geoscience Map 2014-03, scale 1:150000. doi:10.4095/295460
- Roddick, J.A., 1970. Douglas Channel-Hecate Strait map area, British Columbia; Geological Survey of Canada, Paper 7G-41, 56 p.
- Pedersen, G.B.M., and Grosse, P., 2014. Morphometry of subaerial shield volcanoes and glaciovolcanoes from Reykjanes Peninsula, Iceland: Effects of eruption environment; *Journal of Volcanology and Geothermal Research*, v. 282, p. 115–133.
- Porter, S.C., 1972. Distribution, morphology, and size frequency of cinder cones on Mauna Kea Volcano, Hawaii; *Geological Society of America Bulletin*, v. 83(12), p. 3607–3612.
- Rohr, K.M.M., and Dietrich, J.R., 1992. Strike-slip tectonics and development of the Tertiary Queen Charlotte basin, offshore western Canada: Evidence from seismic reflection data; *Basin Research*, v. 4., p. 1–19.
- Russell, J.K., Edwards, B.R., Porritt L., and Ryane, C., 2014. Tuya: a descriptive genetic classification; *Quaternary Science Reviews*, v. 87, p.70–81. doi.org/10.1016/j.quascirev.2014.01.001
- Schilling, D.H., and Hollin, J.T., 1981. Numerical reconstructions of valley glaciers and small ice caps; *in* The last ice sheets, (ed.) G.H. Denton and T.J. Hughes, John Wiley and Sons, New York. p. 207–220.
- Slaymaker, O., and Kovanen, D.J., 2016. Pleistocene landscapes of western Canada; *in* Landforms and Landscapes of Western Canada, (ed.) O. Slaymaker, Springer, p. 27–48.
- Smellie, J. L., 2007. Glacial landforms/Quaternary vulcanism, subglacial landforms; *in* Encyclopedia of Quaternary Science, (ed.) S.A. Elias, Elsevier, p. 784–798.
- Souther, J.G., 1992. Milbanke Sound Cones, Canada; *in* Volcanoes of North America: United States and Canada, (ed.) C.A. Wood and J. Kienle, Cambridge University Press, Nature, p. 130–131.
- Yamagishi, H., 1991. Morphological and sedimentological characteristics of the Neogene submarine coherent lavas and hyaloclastites in Southwest Hokkaido, Japan; *Sedimentary Geology*, v. 74, p. 5–23.
- Wheeler, J.O., Brookfield, A.J., Gabrielse, H., Monger, J.W.H., Tipper, H.W., and Woodsworth, G.J., 1991. Terrane map of the Canadian Cordillera; Geological Survey of Canada Map 1713A, 1:2 000 000 scale.
- Wood, C.A., 1980a. Morphometric evolution of cinder cones; *Journal of Volcanology and Geothermal Research*, v. 7, p. 387–413.
- Wood, C.A., 1980b. Morphometric analysis of cinder cone degradation; *Journal of Volcanology and Geothermal Research*, v. 8, p. 137–160.
- Woodsworth. G.J., 1991. Neogene to Recent volcanism along the east side of Hecate Strait, British Columbia; *in* Evolution and Hydrocarbon Potential of the Queen Charlotte Basin, British Columbia,



Geological Survey of Canada. Paper 90-10,  
p. 325-335.

## Appendix 1 – Petrographic Notes – Kitasu Hill Thin Sections

Notes by T.S. Hamilton

### Sample 17-BJB-001 (Figures 1-1 to 1-4)

Highly vesiculated basaltic foam (~50%). Flow oriented microlites of plagioclase (Fig. 1-1). Euhedral birefringent phenocrysts of olivine (Figs. 1-2 and 1-3) and augite (Fig. 1-3). Phenocrysts of grey-white reflected cubic magnetite (~5%, Fig. 1-4), some with spongy resorbed rims and inclusions of bright creamy white ilmenite (<1%) (xenocryst?). Olivine, fractured, highly birefringent, high relief with wedge-shaped, 6 sided or parallel-sided prismatic sections (parallel extinction) in rectangular laths. Black groundmass glass (~25%, Figs. 1-3 and 1-4)), the rest is plagioclase, olivine, augite, and magnetite. Magnetite has cubic to triangular sections. Orange hematite/limonite fractures in olivine and rims in larger vesicles (Fig. 1-3, water present at quench). Plagioclase phenocrysts (as well as large olivines) all have intimate reticulate fractures (Fig. 1-3) as if hot large crystals shrank and fractured in water.

Largest plagioclase phenocrysts (0.7 mm) are glomerocrysts with strong Ca → Na zonation then resorption and reset calcic rims with 7° core to rim angle change for extinction. (large  $52^\circ/2=26^\circ$ , small  $8^\circ$  An80 ← units core)

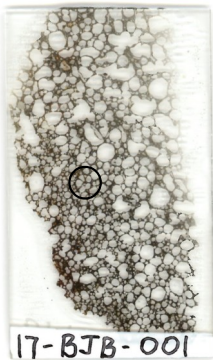


**Figure 1-1.** Thin section Sample 17-BJB-001, 46x26 mm. Highly vesiculated basaltic foam (>50%). Vesicles to 4 mm rounded, subrounded and agglutinated. Segregated regions of larger abundant and smaller less abundant vesicles with dark basaltic glass host. The circle corresponds to Fig. 1-2.

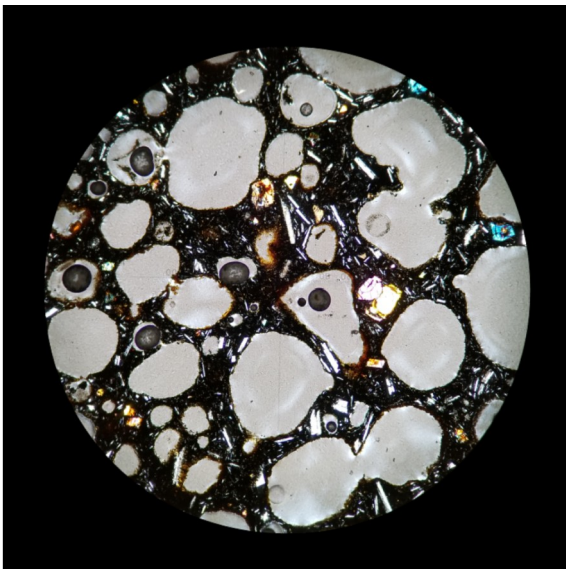


**Figure 1-2.** Crossed polarized light (XPL) of sample 17-BJB-001, ~ 4.5 mm diameter field of view (FOV). Average vesicle size < 2mm. Flow oriented plagioclase microlites, fractured highly birefringent olivine and augite in dark basaltic glass groundmass. Plagioclase is ~3 times more abundant than olivine.

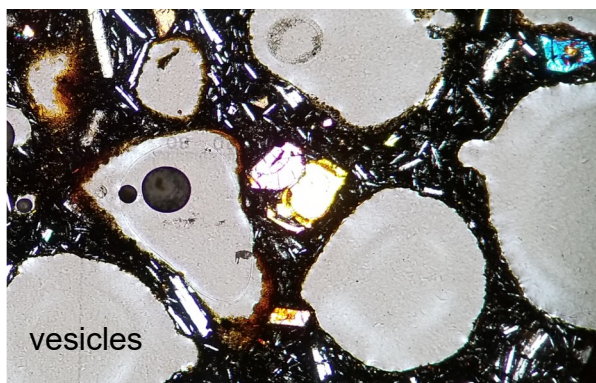


**Figure 1-3.** Close up of right center portion of Fig. 1-2, XPL, FOV 2.4x1.66 mm. Plagioclase is long and narrow tabular to needle like crystals. Olivine has high relief and high birefringence here yellow to blue with wedge shaped to parallel sided prismatic crystals. Note plagioclase micro-lites have prongs on end. Olivines are subhedral partial hopper crystals and fractured. All 3 of these textures indicate crystal growth and thermal shrinkage during rapid quenching.

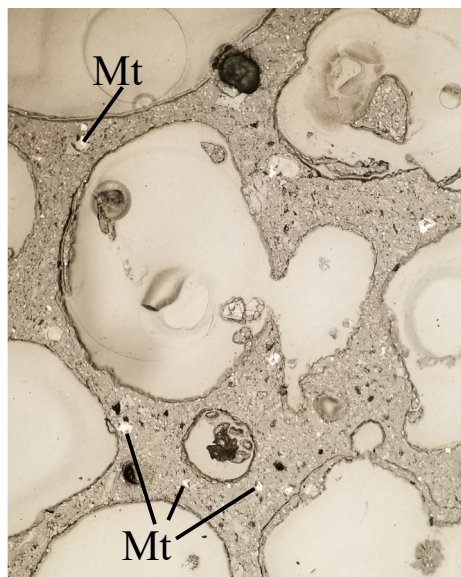


**Figure 1-4.** Different area of 17-BJB-001, RPL with FOV 2.54x2.03 mm. Glassy groundmass is translucent with abundant microlites. Vesicles ~2 mm show glassy linings and microlite growth into cavities suggesting rapid quench below glass transition temperature. Microphenocrysts of magnetite show as intensely white reflective euhedral squares and triangles to 5 µm.

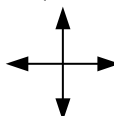
## Sample 17-BJB-002 (Figures 2-1 to 2-6)

White plagioclase laths, birefringent olivine.

Dense flow-aligned plagioclase phenocrysts to 4×1 mm.

Crystallization order as slide 001: olivine 1<sup>st</sup>, plagioclase 2<sup>nd</sup>, augite 3<sup>rd</sup>; magnetite throughout and 4<sup>th</sup> in groundmass glass and against silicate phenocryst phases (late stage water build up and oxidation).

Abundance: plagioclase > augite > olivine phenocrysts; Magnetite cubic grains form phenocrysts and groundmass disseminated cubic to dendritic (wires, dendrites, needles) implying rapid cooling rate, Olivine has hopper crystals, optic axis/Bxa on figure, low



symmetric extinction, birefringence section, fractured 6 sided to rounded.

Plagioclase is up to a few mm in size with An72 core.

Some of the largest plagioclase have resorbed rims and glass in rims and fractures.

Magnetite ~5% late stage oxide rims on glass/phenocryst boundary and microlites implying H<sub>2</sub>O built up and late oxidation of quench. Basalt is dense and, other than plucking in making the thin section, is hard/quenched during flow.



**Figure 2-1.** Thin section 17-BJB-002, 46x26 mm. Dense dark grey, very fine grained, flow aligned basalt with resorbed plagioclase megacrysts to 3.5 mm long. White circle shows location of Fig. 2-2.



**Figure 2-2.** Thin section 17-BJB-002, XPL, FOV 4.5 mm. Flow aligned plagioclase crystals. Larger xenocryst as per Fig. 2-1, has resorbed edge and brownish birefringence due to being too thick. Cumulophyric aggregate of euhedral olivine with yellow to 3<sup>rd</sup> green birefringence in lower right corner. Plagioclase is ~4x more abundant than olivine. Dark basaltic groundmass glass ~20% of FOV.

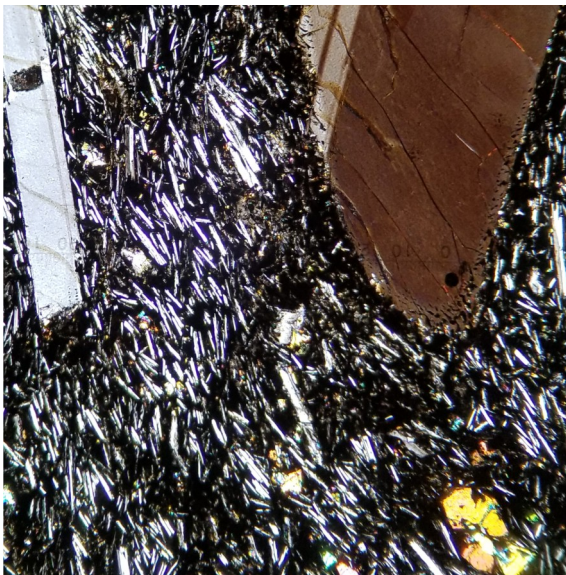


**Figure 2-3.** Expanded view of Figure 2-2 above. Thin section 17-BJB-002, XPL, FOV 2.9 mm square. Brown birefringent embayed plagioclase megacryst has thin remelting and reaction rim. Due to having albite and Carlsbad albite twin laws at an acute angle ~10° this is likely a composite grain inherited from the coast range plutonic rocks at depth.



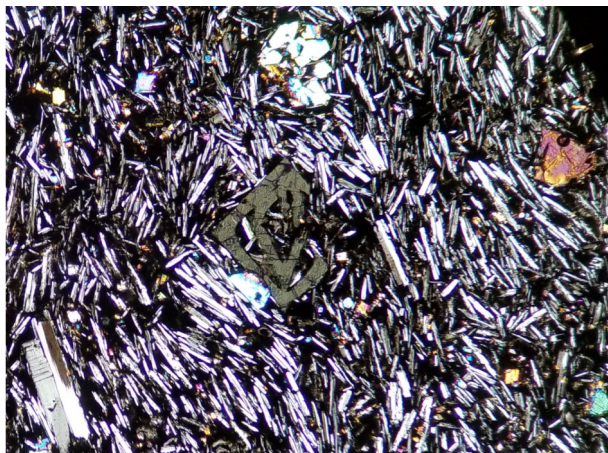


**Figure 2-4.** Thin section 17-BJB-002, XPL, FOV 2x2.5 mm. Plagioclase microlites are diagonally flow aligned. Largest microphenocrysts have An<sub>76</sub> cores. Olivine occurs as birefringent high relief wedges and diamond-shaped euhedra, cumulophyric aggregates and a few hollow cored hopper crystals indicating rapid quench rates during crystallization (see crystal with grey birefringence near centre of image ~53  $\mu$ m across).

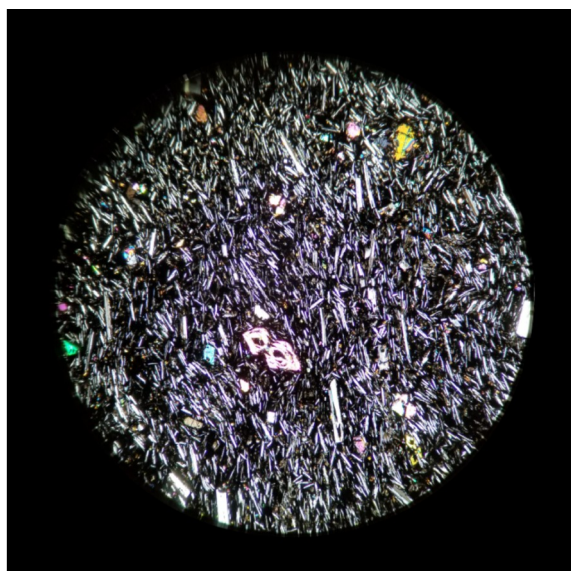


**Figure 2-5.** Thin section 17-BJB-002, XPL, FOV 4.5 mm. Different area than Figure 2.2 above. Vertically aligned plagioclase microlites with composite hopper crystal of olivine (owl's mask) near centre of field. Hopper crystal and fine microlites indicate rapid quenching.

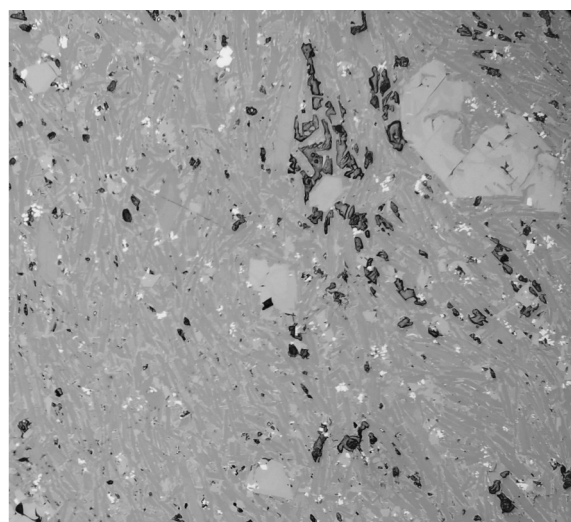


**Figure 2-6.** Different area of 17-BJB-002, RPL with FOV 2x1.8 mm. Olivines euhedral and high relief to ~50  $\mu$ m. Plagioclase forms smaller laths with light grey reflectance. Magnetite is euhedral, bright white reflectance and < 2  $\mu$ m, ~2%. Abundant grey groundmass basaltic glass. Darkest areas are plucking from polished thin section preparation.

## Sample 17-BJB-003 (Figures 3-1 to 3-3)

Dense basalt.

Order of crystallization: Olivine 1<sup>st</sup> > plagioclase 2<sup>nd</sup> > augite 3<sup>rd</sup>; Magnetite last in glass.

← equant →                      subequant  
largest to 2 mm, most abundant

~30% brown glass in groundmass.

Olivine has highly birefringent hopper crystals (hollow cores); with some bladed growths from rims on largest 2 mm phenocrysts (quench texture).

Magnetite is cubic to dendritic, forms in the bulk of the rock, and films on boundary of the groundmass glass against phenocrysts as per 17-BJB-002. This texture implies rapid hydration, oxidation and quenching.

This section has lots of plucking (of glass and a few tabular plagioclase phenocrysts) and abundant >30% groundmass glass. There are also some glomerocrysts of cognate xenoliths or xenocrysts of olivine and plagioclase.

### *General Comment*

Rocks/flows 17-BJB-002 and 003 are very similar and closely related to 001 scoria, if not all cogenetic and very closely sequential from a single batch of hot, relatively primitive olivine basalt or alkali-olivine basalt magma. This is typical of intraplate Cordilleran settings with shallow asthenosphere (~19 km under Hecate Strait). Here, there is little mantle lithosphere and crust in tension. Magmas form readily with small amounts of adiabatic decompression melting such as from rebound.



**Figure 3-1.** Thin section 17-BJB-003, 46×26 mm. Dense dark grey, very fine grained, flow aligned basalt with rare resorbed plagioclase megacrysts to 2 mm. Mostly dark dense basaltic glass. White circle shows location of Fig. 3-2.

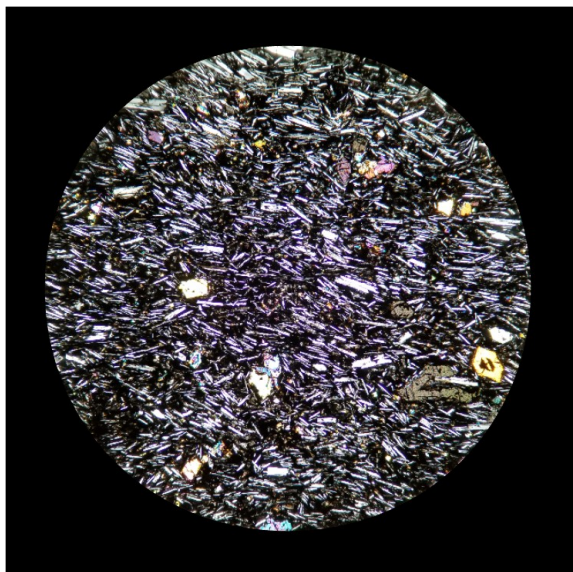


**Figure 3-2.** Sample 17-BJB-003, 4.5 mm FOV, XPL. Plagioclase 4x Olivine abundance. Plagioclase is flow aligned E-W. Microlites to felted intersertal habit for plagioclase groundmass intergrown with dark basaltic glass. Olivines are euhehedral and hopper shaped (lower right edge) indicating rapid quenching.

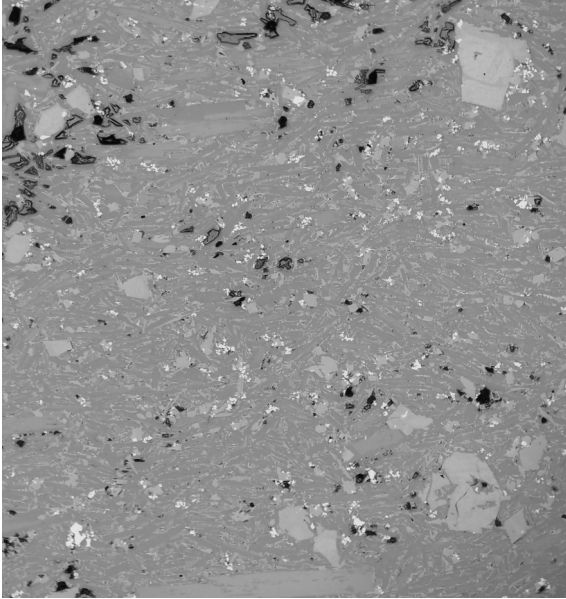


**Figure 3-3.** Different area of 17-BJB-003 RPL with FOV 2.26x2.14 mm. Larger microphenocrysts of clear euhedral olivine are prominent and ~10 of area. Black spots are plucks, holes in the section. Magnetite is highly reflective white and euhedral (e.g. lower left corner and disseminated throughout. Magnetite is ~2% of FOV in sub 2  $\mu$ m size range.

### **Sample 17-BJB-004** (Figures 4-1 to 4-6)

Mildly vesicular, somewhat glassy (~20%) olivine basalt or alkali olivine basalt.

Crystallization order: olivine 1<sup>st</sup> > plagioclase 2<sup>nd</sup> > augite 3<sup>rd</sup>. Magnetite inclusions in olivine and plagioclase phenocrysts → and late as microscopic <2  $\mu$ m highly reflective grayish white disseminations, wires, dendrites and cubes in groundmass glass.

Olivine is fractured and occurs as phenocrysts or as hopper crystals. Plagioclase phenocrysts are fractured.

Magnetite crystallized with high temperature silicates and formed as tiny crystals on contacts of glass with crystals (e.g. plagioclase, olivine, etc.). This implies late H<sub>2</sub>O buildup and oxidative quench as per samples 002 and 003. Section 004 has more altered glass than 002, 003 and hematite/limonite with iron hydroxide spherules to 0.5 mm.

Augite forms blades on, and from, earlier plagioclase phenocrysts at final quench (feathery blades with inclined extinction). This is a rapid quench texture (strong undercooling) with rapid cooling, similar to 001. Quench rate is less than 001 but more than 002 or 003.

Quench and devitrification makes very ragged rims and overgrowths on plagioclase phenocrysts.

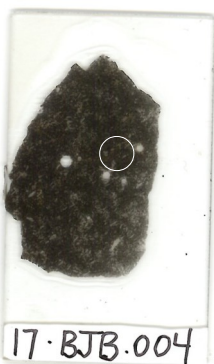


**Figure 4-1.** Thin section 17-BJB-004, 46×26 mm. This lava is fairly dense dark grey, very fine grained and flow aligned basalt with sparse rounded vesicles to 1 mm. Dark basaltic glass dominates. White circle shows location of Fig. 4-2.



### *General Comment*

These are all olivine basalts or alkali olivine basalts that are typical of within-plate, mantle-derived dry magmas from a small percentage of partial melting. Petrographically they all look similar and mafic (high Mg number or high NBO/T from water dissociation?) like oceanites and highly olivine phyric basalts from the Reykjanes peninsula. They all have abundant olivine, augite, magnetite and brown glass. The preservation of the olivine and glass is excellent and demonstrates that they are young and have been kept from any significant weathering.

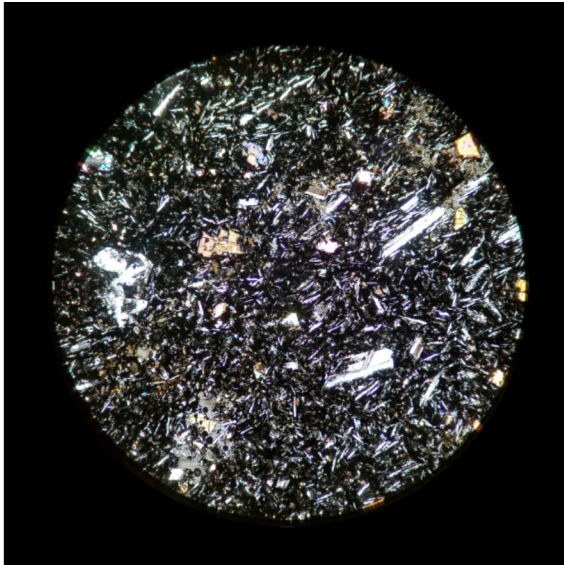


**Figure 4-2.** 17-BJB-004, 4.5 mm FOV, XPL. Plagioclase 4x Olivine with yellow birefringence is abundant with lesser augite and dark groundmass basaltic glass. Partial flow alignment of plagioclase microlites NE-SW.

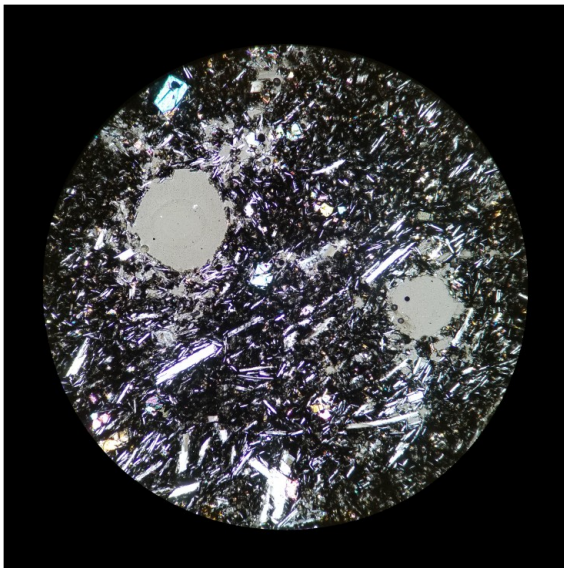


**Figure 4-3.** 17-BJB-004, 4.5 mm FOV, XPL, immediately below Figure 4-2. Plagioclase has 4x Olivine abundance. Olivine occurs as fractured euhedral triangles and rectangles in lower left. Micro-lites to felted intersertal habit for plagioclase with feathery overgrowths of augite with inclined extinction. Minor residual dark basaltic glass < 10%.

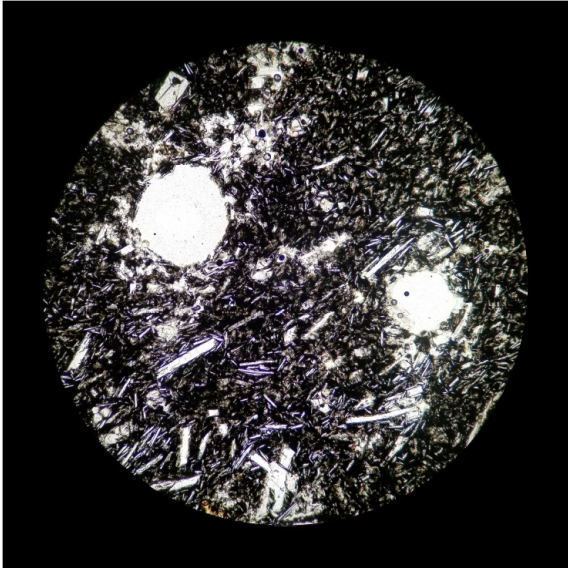


**Figure 4-4.** 17-BJB-004, 4.5 mm FOV, PPL of same area as Figure 4-3. Plagioclase 4x olivine abundance. Microlites to felted intersertal habit for plagioclase with feathery overgrowths of augite with inclined extinction. Minor residual dark basaltic glass < 10%. Olivines are euhedral and hopper shaped indicating rapid quenching. Olivine has inclusions of magnetite and microscopic magnetite overgrowths. This sample has more altered glass with hematite and limonite. Textures indicate this sample had rapid quenching, less than 001 but more than 002 or 003. Some vesicles are slightly lined by chlorite spherules, showing subsolidus hydrous alteration.

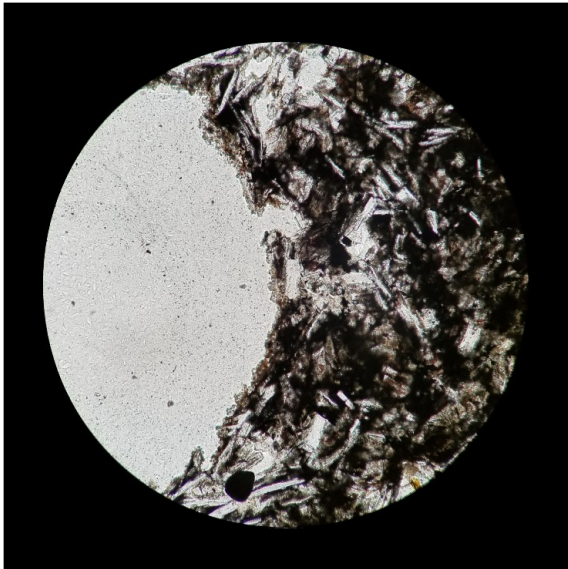


**Figure 4-5.** 17-BJB-004, 1.08 mm FOV, closeup of Figure 4-4 above, PPL near the right side of the upper vesicle. Note large opaque sub-rounded magnetite inclusion in lower field of view. Likely xenocryst from plutonic basement rocks.

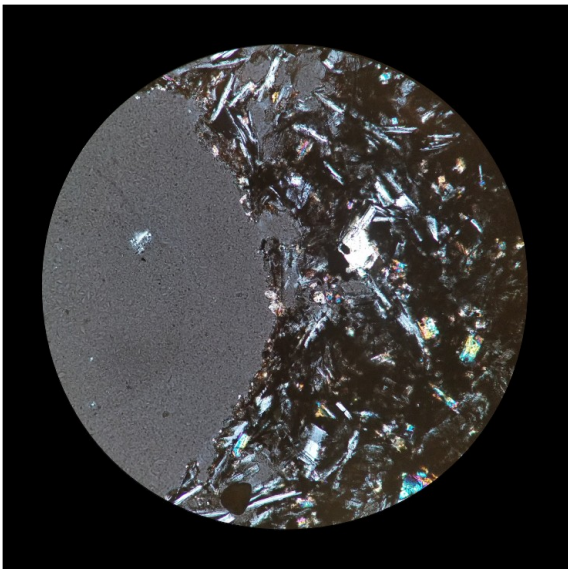


**Figure 4-6.** 17-BJB-004, 1.54 mm FOV, as Figure 4-5 above, XPL. Note fractured highly birefringent olivines and microlites as quench lining in vesicle walls.

## Sample 17-BJB-005 (Figures 5-1 to 5-15)

This is a diamict. Even in this single thin section sized sample there are abundant:

Volcanics (volcanic rock fragments (VRF), palagonite and brown glass) dominate (~80%) with clasts  $\geq 4$  mm.

Plutonic rock fragments (PRF) and Plutonic derived minerals comprise ~20%.

All the textures and minerals in the VRFs are identical and clearly come from a common volcanic source like thin sections 17-BJB-001 to 004 inclusive. These flows are cogenetic with the glacial sediment being time-tied to the volcanism because of the preservation of brown glass and unweathered olivine and little rounding or transport and poor sorting.

The diamict formed dominantly from volcanic debris and volcanism with lesser contributions of ice rafted debris or glacial sediment load sourced from the Coast Plutonic complex. Plutonic rock fragments are mostly hornblende – biotite – granodiorite and granite. These plutonic rock fragments have exolved magnetites with ilmenite. The Hornblende has a predominantly green pleochroic formula. The biotite has a brown pleochroic formula. There is some sericite and structural deformation of granodiorite that occurred at a late intrusive phase in the source pluton.

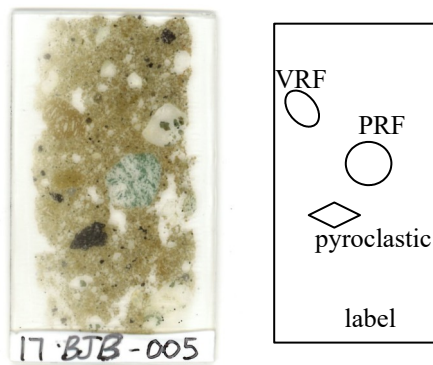


**Figure 5-1.** Thin section 17-BJB-005, 46x26 mm. Diamict texture from  $> 1$  cm lithic pebbles (as shown 7 mm) to silt and mud size matrix. VRF clasts dominate with lesser plutonics and large diverse plutonic mineral fragments. Greenish brown colour is due to abundant, reduced, volcanic glass in the silt size range.

Some volcanic rock fragments are dominantly glass. This is unusual in sediments as glass is soft and susceptible to abrasion during transport and chemically highly unstable.

In this sediment, the abundance order is: brown glass  $>$  plagioclase  $>$  olivine  $>$  augite  $>$  magnetite. Quenched glass is abundant in large pyroclasts and as matrix debris. Olivine is hopper shaped with quench textures. Olivine almost never survives transport and deposition unless it is sealed in when deposited and water is kept away. Some brown glass is fresh, in other clasts the glass is palagonitized (bathed in boiling hot water).

There are three distinct glass types preserved in this sample:

- 1) Large clear brown freshly quenched basaltic glass (60% of fragment) with trapped silicate and oxide phenocrysts. This is identical to samples 002 and 003 but there was insufficient time to crystallize or oxidize the groundmass glass so the samples in this sediment were thoroughly quenched as the magma came out.
- 2) Basaltic rock fragments with altered opaque black glassy groundmass ~20% like samples 001 through 004.
- 3) Palagonite – orange brown, bubbly translucent – poor continuity, small domains up to  $\sim 5$   $\mu$ m across and rims inside vesicles. Smaller fragments and incipient alteration where water/stream contacted glass.



Two things clench this as a volcano-glacial diamict: 1) the abundance of glass with varied textures, and 2) the presence of relatively fresh olivine. Neither of these survive aqueous transport and redeposition, which indicates very rapid quenching and deposition and the material's burial in situ. This sample is reminiscent of many Quaternary tuya samples elsewhere in BC/Cordillera.

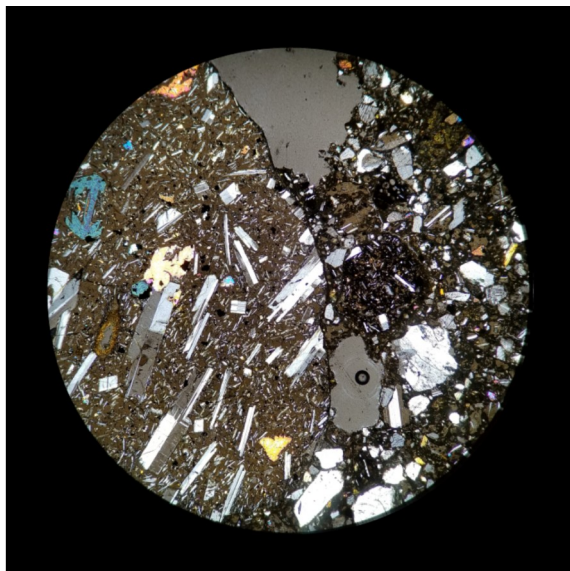


**Figure 5-2.** 17-BJB-005, 4.5 mm FOV, XPL. Left side of image is a single rounded basaltic pyroclastic fragment with well-preserved, unaltered 55% brown basaltic glassy groundmass. Plagioclase is 4x olivine. Olivine shows incomplete euhedral, fragile, hopper crystals. This VRF has a higher quench rate than samples 17-BJB-001 or 002. Right side of image is predominantly altered green brown glass with 5 mm to 12 mm plutonic quartz and plagioclase with interlocking grain boundaries. Along with the altered silt size glass, there is 5-10% highly birefringent ferromagnesian minerals including olivine, hornblende and epidote. Preservation of fresh brown glass and abundant glass as sedimentary load implies little or no transport or redeposition. The preservation of detrital olivine is rare in sediments and fresh glass only occurs close to a volcanic vent with rapid burial and cementation.

The presence of plutonic load from hornblende granodiorite implies glacial load added and admixed with the volcanics at the time of deposition with little sorting or maturation of particles by size, shape, composition, mechanical or chemical durability.



**Figure 5-3.** 17-BJB-005, 1.4x2.2 mm FOV, XPL. Expanded view of the left edge of Fig. 5-2 above. Birefringent hopper crystals of olivine, laths of plagioclase and matrix of brown glass dominate the image. The olivine hopper form denotes fast quenching. Preservation of olivine and basaltic glass show rapid deposition from basaltic source with no reworking.

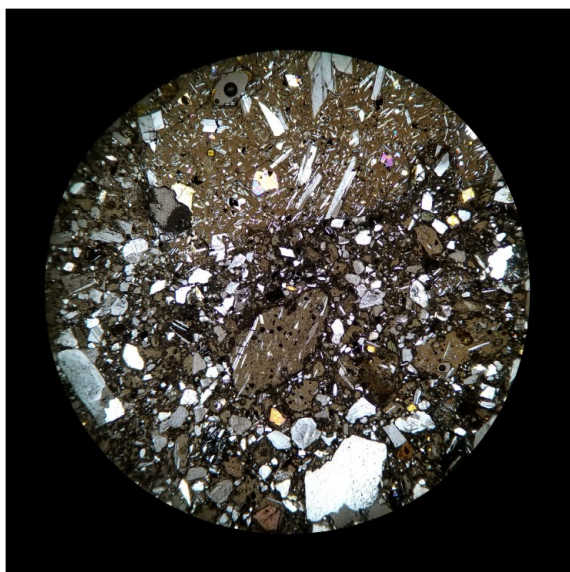


**Figure 5-4.** 17-BJB-005, 4.5 mm FOV, XPL. The central upper edge of this figure overlaps slightly with the left edge of Fig. 5-2. Pyroclastic glassy volcanic rock fragments dominate sedimentary particles from pebbles to silt. There is also abundant but lesser plutonic sutured quartz, plagioclase and hornblende in large mineral crystals and plutonic rock fragments.

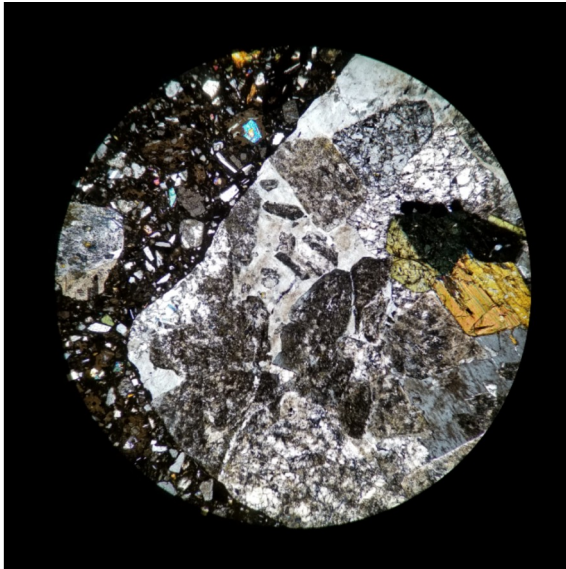


**Figure 5-5.** 17-BJB-005, 4.5 mm FOV, XPL. Different area than Figs. 5-2 through 5-4. The two large rock fragments are plutonic with euhedral prismatic hornblende and interlocking quartz, orthoclase, plagioclase and magnetite. The matrix also has plutonic quartz and feldspars but still has predominant basaltic glass, volcanic plagioclase and olivine.

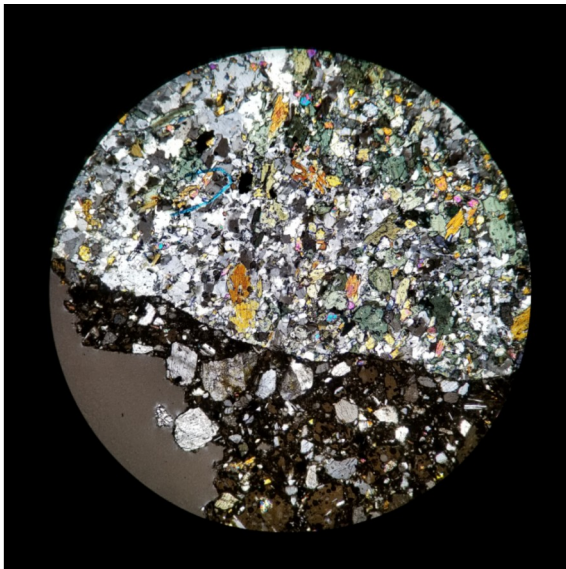


**Figure 5-6.** 17-BJB-005, 4.5 mm FOV, XPL. Different area than Figs. 5-2 through 5-5. A plutonic rock fragment of hornblende granodiorite dominates the upper field of view. The matrix has plutonic quartz and feldspars but still has predominant basaltic glass, volcanic plagioclase and olivine as in Fig. 5-5.

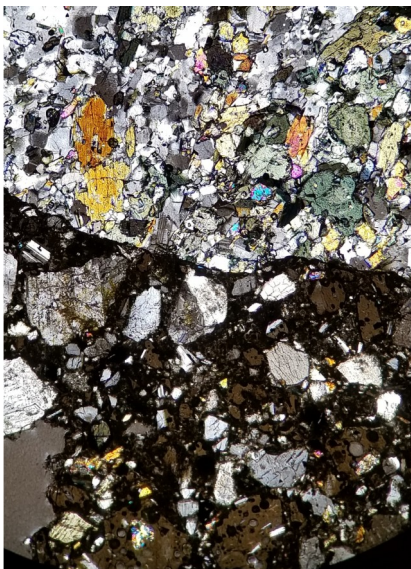


**Figure 5-7.** 17-BJB-005, 2.07×2.85 mm FOV, XPL. Expanded view of Fig. 5-6. Rounded plutonic rock fragment of hornblende granodiorite and mineral load of plutonic feldspars and quartz comprise the larger sand size grains. Matrix is predominantly basaltic glass. This sample shows admixture of fresh basaltic material and reworked plutonic glacial debris.



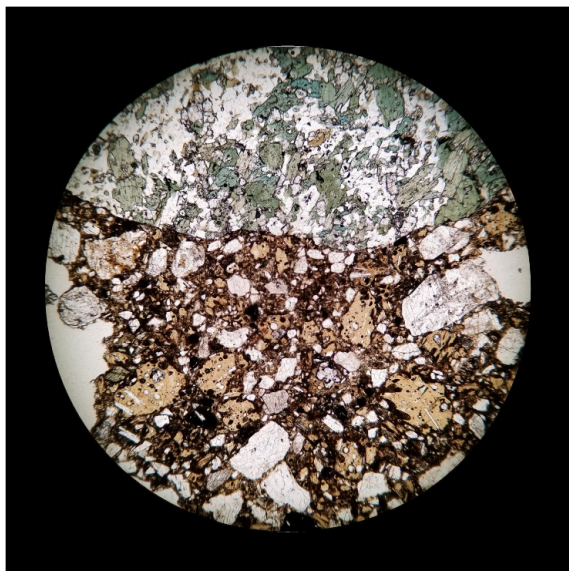


**Figure 5-8.** 17-BJB-005, 4.5 mm FOV, PPL. The figure overlaps with Figs. 5-6 and 5-7. The largest rounded rock fragment is plutonic diorite with hornblende having a green pleochroic formula and distinctive large opaque magnetite crystals surrounded by clear feldspars and quartz. The smaller yellowish angular to subangular grains are slightly devitrified basaltic glass (VRFs).



**Figure 5-9.** 17-BJB-005, 1.15 mm FOV, PPL. Expanded view right part of Figure 5-8. Subrounded clear PRF's dominate the image. A large brown subangular VRF near the centre shows preservation of fresh basaltic glass along with smaller glassy VRF's and much of the matrix indicating rapid quenching and deposition with little or no reworking.

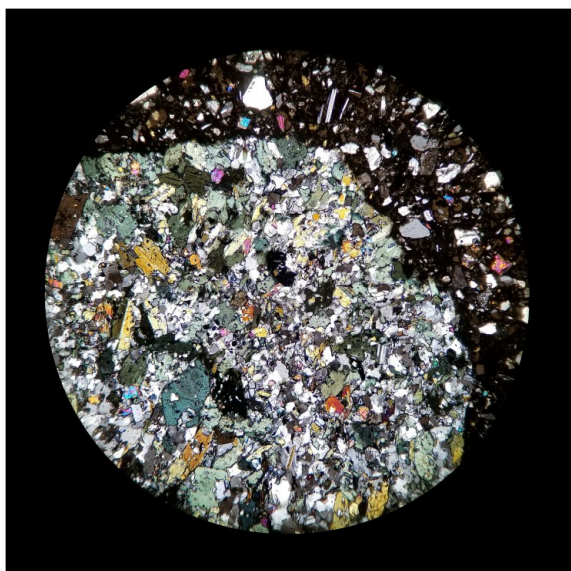


**Figure 5-10.** 17-BJB-005, 4.5 mm FOV, XPL. Different area than Figures 5-2 to 5-9 above. Similar to Figure 5-5 in showing glacially derived plutonic rock and mineral fragments in a matrix with substantial basaltic glass.

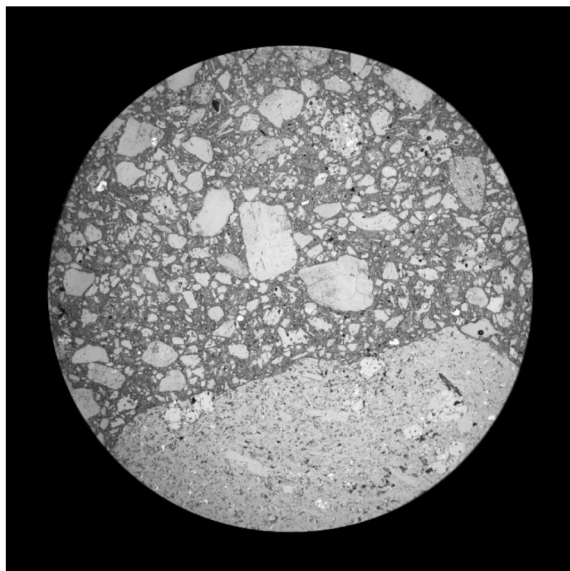


**Figure 5-11.** 17-BJB-005, 4.5 mm FOV, RPL. Different area than Figs. 5-2 to 5-9. Sand sized silicate rock and mineral fragments dominate with lesser dark basaltic glass in matrix. The 2 bright white grains near the upper left are detrital magnetite from plutonic sources. The poor sorting of the diamict is readily apparent.

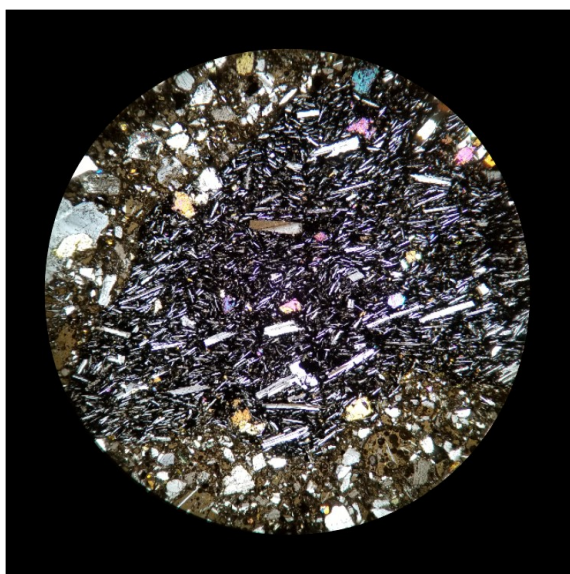


**Figure 5-12.** 17-BJB-005, 4.5 mm FOV, XPL. Here a fine grained flow aligned plagioclase in a volcanic rock fragment equal to the Kitasu Hill Basalt samples (17-BJB-001 through 004) occupies the centre of the image. Plutonic quartz, feldspar and hornblende minerals along with brown basaltic glass fragments comprise the surrounding matrix.

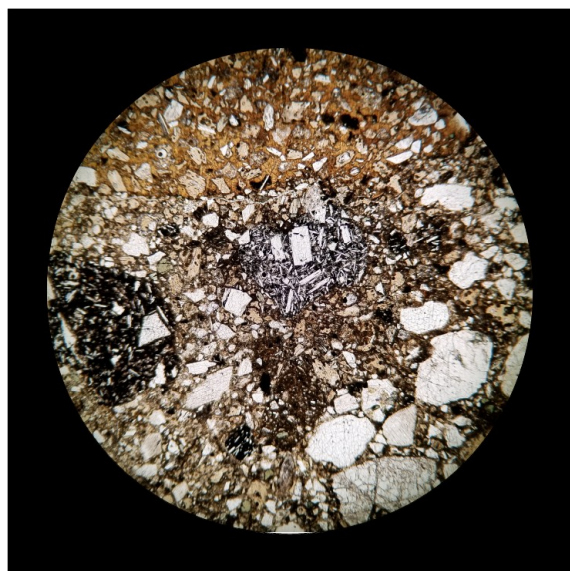


**Figure 5-13.** 17-BJB-005, 4.5 mm FOV, PPL. The lower part of the image slightly overlaps the upper part of Fig. 5-11. Large lithic fragments in upper left image are VRF's of varying opacity and alteration for their glassy groundmass. Most mineral grains in the lower right are clear plutonic feldspars and quartz. Some of the alkali feldspars are turbid or exolved. The matrix is predominantly dark basaltic glass. The sample shows admixture of volcanic and glacially derived plutonic load. Poor grain sorting and little rounding is apparent.



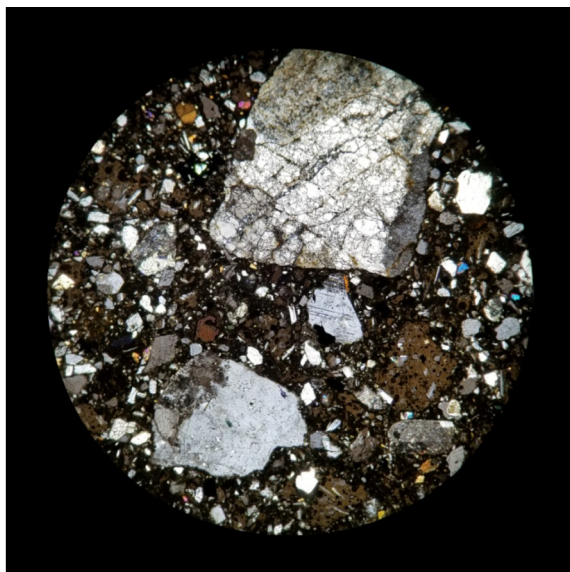


**Figure 5-14.** 17-BJB-005, 4.5 mm FOV, XPL. Different area than Figs. 5-2 to 5-13. Here the largest lithic and mineral fragments are polycrystalline, fractured and zoned plutonic clasts of mainly feldspar and quartz. The matrix contains smaller basaltic rock fragments, brown basaltic glass, olivine, feldspars and hornblende.

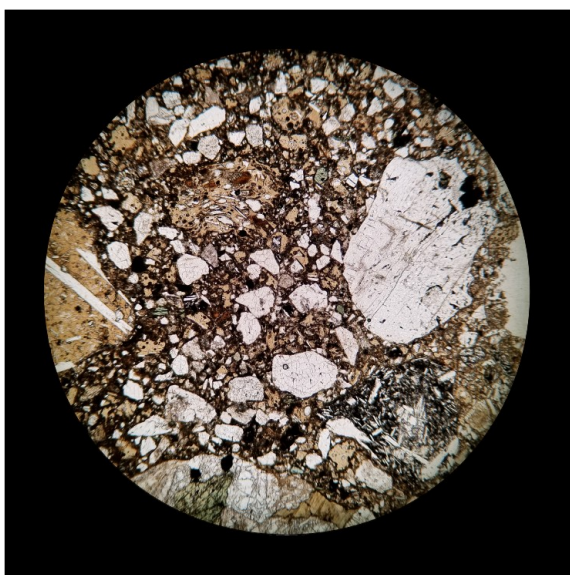


**Figure 5-15.** 17-BJB-005, 4.5 mm FOV, PPL. Different area than Figs. 5-2 to 5-14. Grain supported sandy band with sub-equal plutonic and volcanic derived rock and mineral fragments. VRF's show yellow to clear brown colours in transmitted light indicating variable hydration and alteration. PRF's are clear with large opaque (black) magnetite crystals.

## Sample 17-BJB-006 (Figures 6-1 to 6-10)

This sample is fine sand to silt with a bimodal grain size, fragmented angular grains, minimal rounding. It is grain supported with a mud matrix of about 20%.

Volcanic and plutonic rock fragments dominate the clasts.

VRFs are abundant with dominant clear unaltered brown glass. Some glass is enveloping plagioclase and olivine as per samples 17-BJB-002 and 003.

Mineral sand proportions are plagioclase and alkali feldspar > hornblende > magnetite, rare detrital olivine as mineral fragments and some epidote.

The rock fragments include some plutonic (granodiorite greater than granite), others are intimately fractured volcanic plagioclase so the feldspar textures are distinctive (quench fractured) compared to the clear large optical domains in the plutonic plagioclase. Basaltic VRFs have quenched magnetite in some black/dark devitrified glass like basalts 17-BJB-002 and 003.

The abundance of glass, its good preservation, identical textures to basalt flows and rare dendritic olivine make this sand synvolcanic monogenetic and volcano-glacial origin.

The abundance of zoned and polycrystalline plutonic plagioclase, exolved alkali feldspar with perthite, sutured quartz, hornblende, with large and exolved magnetite, requires some Coast Mountains plutonic sediment load in ice to be melted out and admixed with local volcanic vent sourced basalts and pyroclasts.

### *General Comment*

Samples 17-BJB-002, 003 and 004 are likely subglacial flows or pillow basalts. Sample 17-BJB-001 is a cinder cone scoria probably subaerial. The diamictos 17-BJB-005 and 006 are likely subglacial-glacial-fluvial and syn volcanic.

Deglaciation likely unloaded the local mantle and caused small proportions of partial melting which came up along local faults or tensile fractures through the crust into the base of the diminished ice margin, building the landforms subglacially. The ice was apparently thin enough with respect to the volume of volcanics to melt through to air and allow a build-up of a subaerial cone on top of the planar volcanic platform.



**Figure 6-1.** 17-BJB-006, 4.6×2.6 mm thin section of fractured, silty mud. This sample is matrix supported and has fine sand to silt and a bimodal grain size distribution with a distinct population of larger grains in a finer matrix.



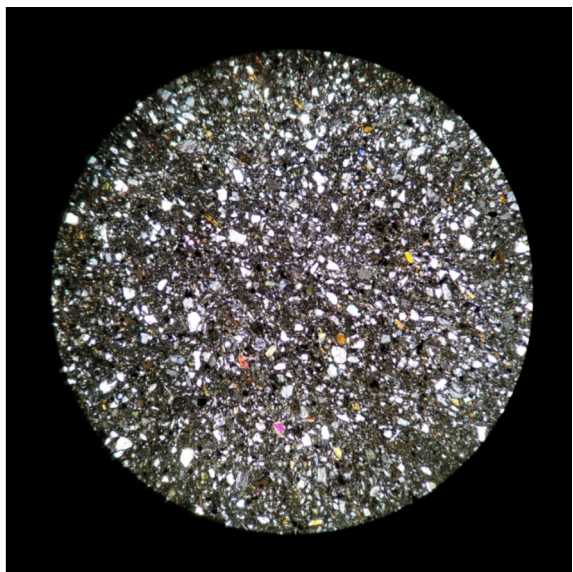


**Figure 6-2.** 17-BJB-006, 4.5 mm FOV, XPL. Fine grained angular to subrounded grain supported sediment. VRF's with clear fresh basaltic glass dominate over plutonic (PRF's). Minerals sand/silt composition is: plagioclase > K-feldspar > hornblende > magnetite > olivine > epidote. The abundance of unaltered glass and quench textured olivine indicate this sediment is synvolcanic and little transported and cemented at the time of deposition to inhibit and water-rock interactions. It is likely waterlain fines transported away from the eruptive source together with subglacial melting.

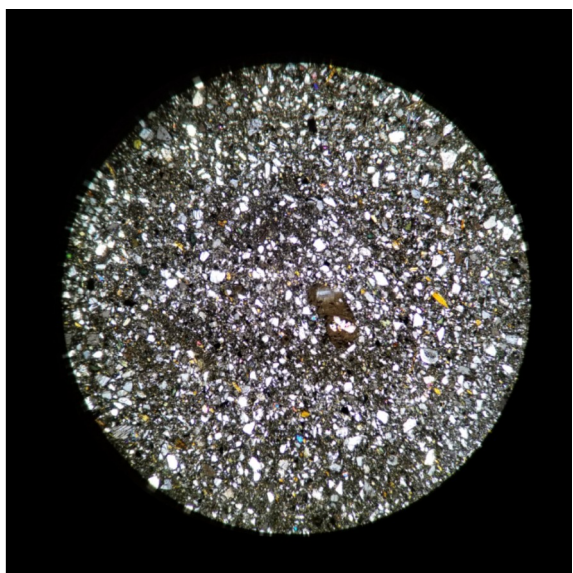


**Figure 6-3.** 17-BJB-006, 4.5 mm FOV, XPL. Figure area overlaps with the top third of Fig. 6-2. As above. Darker patches are dominated by glassy VRF's. Coloured birefringent grains are ferromagnesian minerals: hornblende, olivine and epidote.

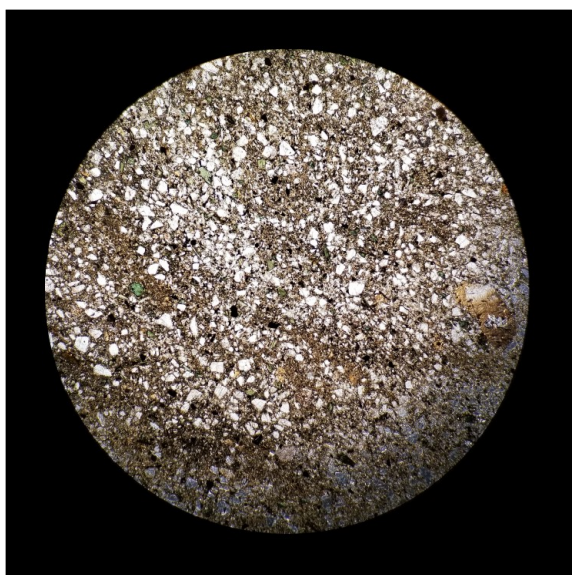


**Figure 6-4.** 17-BJB-006, 4.5 mm FOV, PPL. Figure area overlaps with the left two-thirds of Figure 6-3. Pale green grains are plutonic hornblende. Finer grained dark brown areas are basaltic glass fragments in silt size range. It is a moderately well sorted, semi-layered feldspathic sublithic silt. Detrital plutonic magnetite shows black.

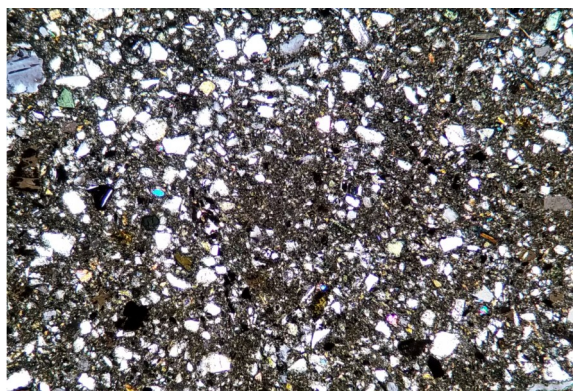


**Figure 6-5.** 17-BJB-006, 2.8x1.6 mm FOV, XPL. Different area than Figures 6-2 to 6-4. Dark (black) grains are detrital plutonic magnetite. Most grains are silicate rock and mineral fragments. This would be classified as an immature feldspathic sublithic grain supported silt. Dense matrix and cements make it impermeable and indurated.

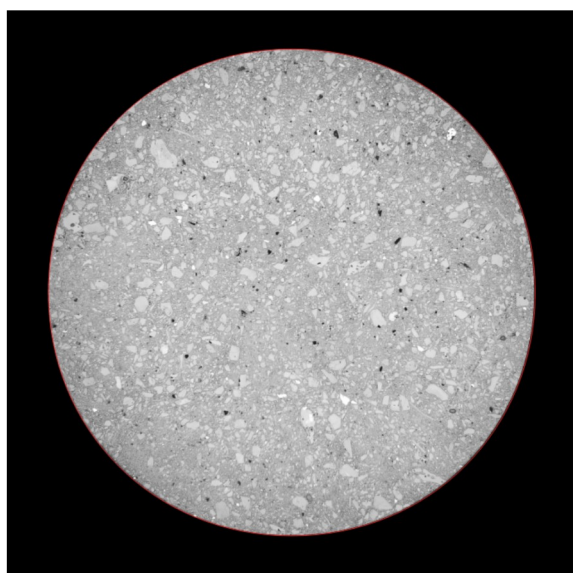


**Figure 6-6.** 17-BJB-006 4.5 mm FOV, PPL. Different area than Figures 6-2 to 6-5. Sparse dark (black) grains are detrital plutonic magnetite. Most grains are silicate rock and mineral fragments. Bimodal grain size and matrix supported texture is apparent.

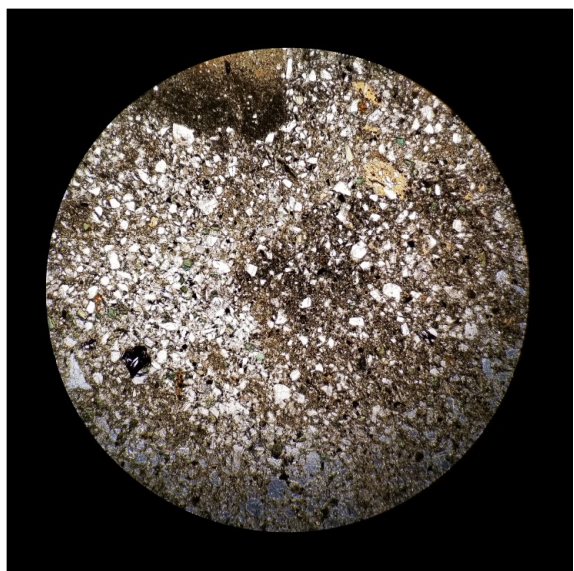


**Figure 6-7.** 17-BJB-006, 4.5 mm FOV, PPL. Different area than Figures 6-2 to 6-6. Largest angular dark brown grain at top of image is a basaltic VRF containing well-preserved groundmass glass. The large black grain to the lower left is an exolved plutonic magnetite grain. Pale green grains are plutonic hornblende. This is a poorly sorted, feldspathic sublithic sandy silt and it is indurated and impermeable.



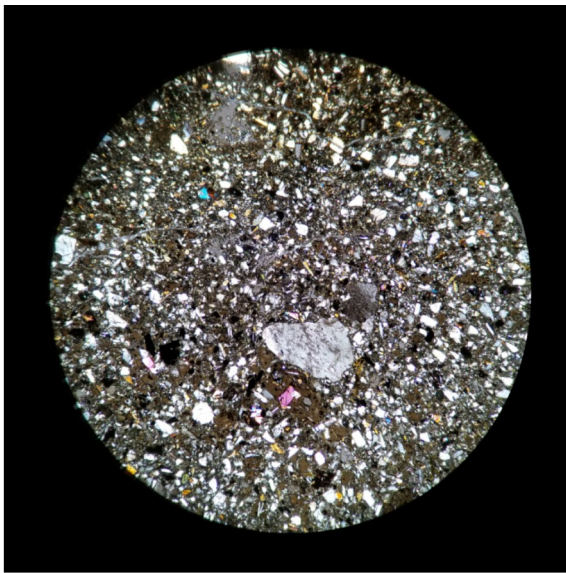


**Figure 6-8.** 17-BJB-006, 4.5 mm FOV, XPL. Different area than Figures 6-2 and 6-7 above. Large grey and white grains are predominantly plutonic feldspars and quartz. Black (opaque) grains are plutonic magnetite. This would be classified as an immature feldspathic sublithic grain supported silt.

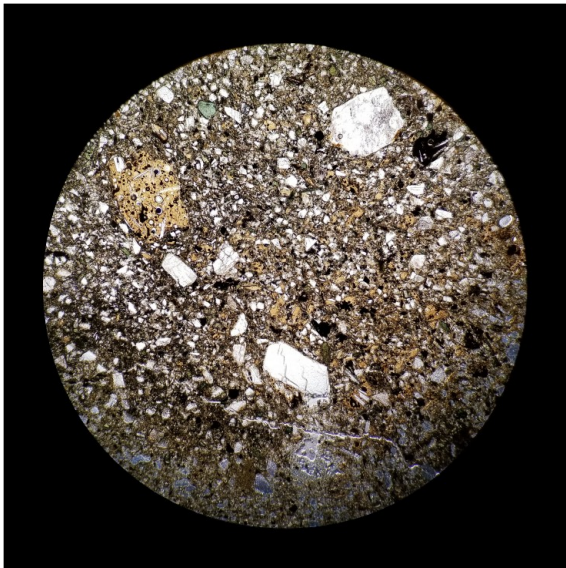


**Figure 6-9.** 17-BJB-006, 4.5 mm FOV, PPL. The figure area overlaps with the top quarter of Figure 6-8. Clear sand grains are plutonic feldspars and PRF's. Yellow grains are VRF's with abundant basaltic glass and some opaque magnetite. Pale green grains are plutonic sourced hornblende. This is a poorly sorted, sandy feldspathic to sublithic silt. Angular grains and glass preservation denote little net transport or reworking. Dense matrix and cement makes it impermeable.

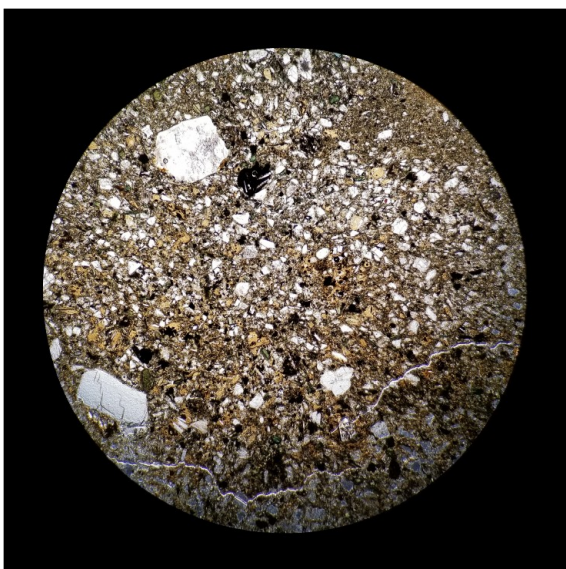


**Figure 6-10.** 17-BJB-006, 4.5 mm FOV, PPL. Overlapping area with the right half of Fig. 6-9 (caption for Figure 6-9).

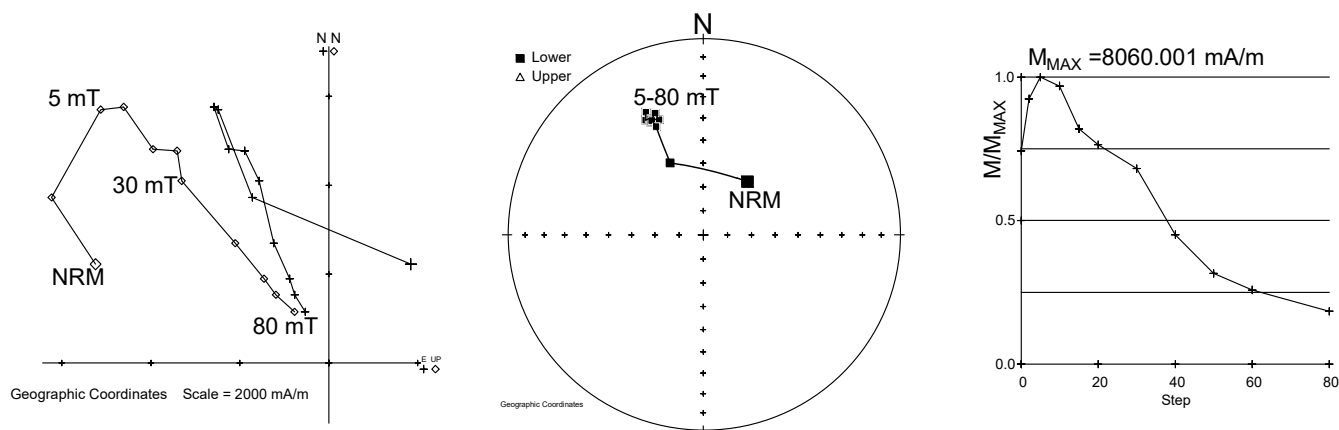
## Appendix 2 – Demagnetization characteristics of the Kitasu basalts

*Comment by R. Enkin:*

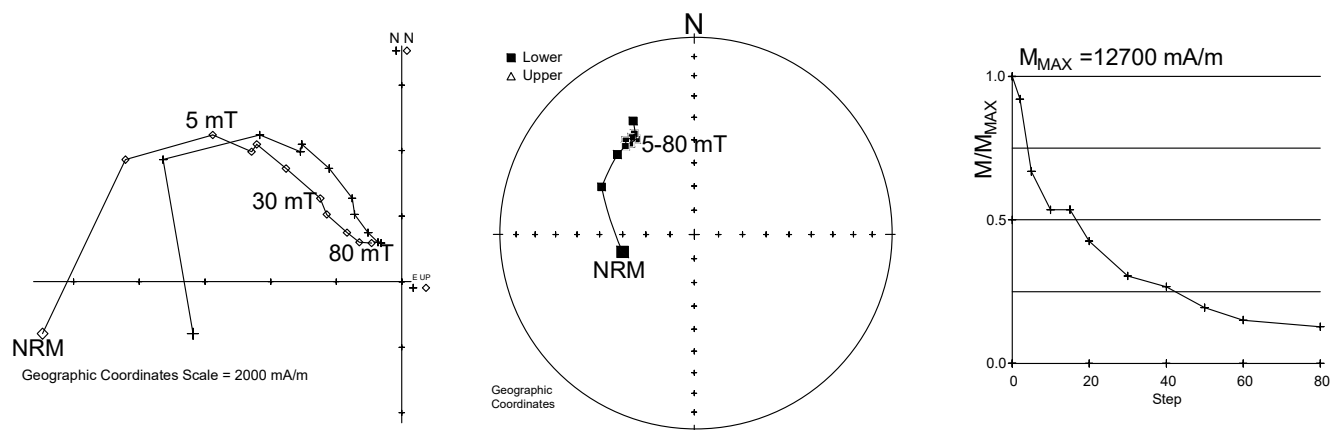
Two samples of dense basalt (17-BJB-003 and 004) both hold primary, stable remanence typical of a magnetic carrier. Both samples hold indistinguishable, but relatively exotic directions. Either they both cooled in a geomagnetic field that was on a big swing of the secular variation (and within at most 100 years of each other, and likely much less), or both sites tilted about 30° down to the SSE. In addition, the two sites likely were overprinted by lightning, or the hand samples received magnetic overprints during shipping. The overprint was easily cleaned, and the high stability component is reliable.

*Orthogonal plot, stereograph, and intensity plot for sample 17-BJB-003 (two specimens).*

BC15421A (field sample 17-BJB-003)



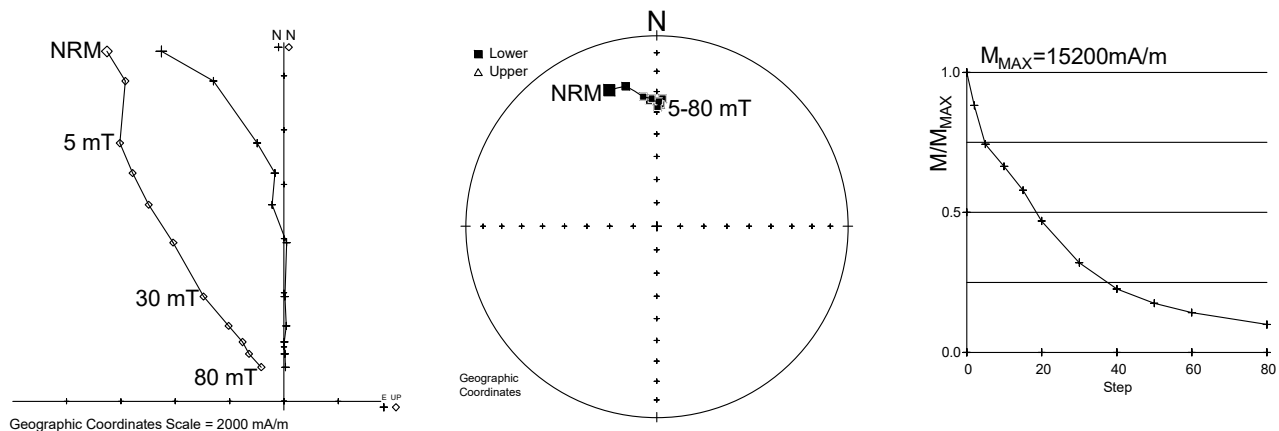
BC15421B (field sample 17-BJB-003)



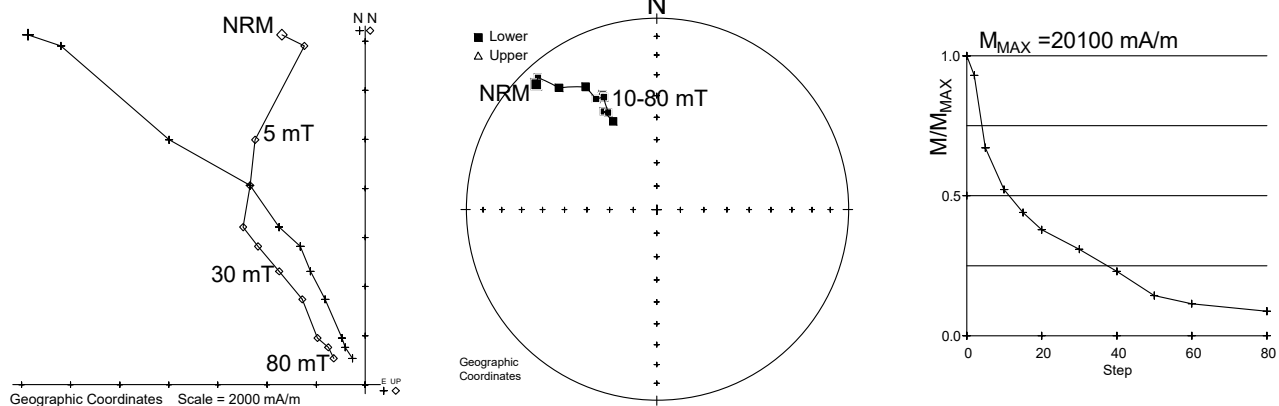


*Orthogonal plot, stereograph, and intensity plot for sample 17-BJB-004 (two specimens).*

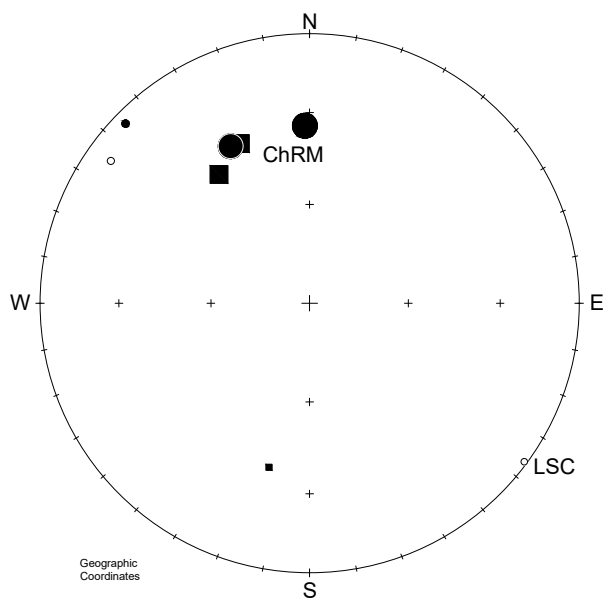
BC15422A (field sample 17-BJB-004)



BC15422B (field sample 17-BJB-004)



*Stable endpoints for all samples.*



Sample: 17-BJB-003 17-BJB-004

Upper  $\square$   $\circ$

Lower  $\blacksquare$   $\bullet$

LSC - Low Stability Component

ChRM - Characteristic Remanent Magnetization

## Appendix 3 – Geochemistry of Kitasu Hill samples

Whole rock characterization with major and trace elements (Table 1) was analyzed by Acme Labs, Vancouver (Bureau Veritas Commodities Canada Ltd.). Analysis included a lithium borate fusion ICP-MS and ICP-ES/MS with a modified aqua regia digestion (1:1:1 HNO<sub>3</sub>:HCl:H<sub>2</sub>O).

Notes from preliminary observations of whole rock geochemistry by T.S. Hamilton

1) The samples, particularly 17-BJB-002, 003 and 004, could all be derived as or from a single batch of magma. Sample 17-BJB-001 may be slightly different due to source heterogeneity or a bit later with a lower degree of partial melting or less differentiation than stratigraphically lower samples or earlier eruptive pulses. (see incompatible elements (item 8 below).

2) As expected the samples are all dry, reduced unaltered basalts that from Alkali Silica and AFM plots classify as Alkali Olivine Basalt to Hawaiite (**Fig. 1**). There is little compositional variation particularly among samples 17-BJB-002, 003 and 004 as determined by replicate analysis. Sample 17-BJB-001 is the most mafic. Raw oxide totals are  $99.36 < \text{Sum.ox} < 100.11$ . Values of  $-0.4 < \text{LOI} < 1.3$  verify that the basalts are all anhydrous and reduced with dominantly ferrous iron. The negative values for LOI (Loss On Ignition) indicate gain of oxygen weight by oxidation on heating rather than driving off of volatiles. Sample 001 which was highly vesicular had the highest LOI at 1.3%. Some of this might have been added H<sub>2</sub>O- weight from cutting the sample wet and incomplete drying or from the tiny proportion of brown weathering rinds inside some of the vesicles along the edges of the cut sample (palagonite clays, iron oxy-hydroxides like limonite or goethite). This is not considered significant or worrisome alteration. There is also no indication of significant water input from glacial meltwater or altered hydrous minerals, in keeping with the abundant basaltic glass both in lava groundmass and in the sedimentary particles within the subglacial sediments.

3) For alkali silica plot classification the SiO<sub>2</sub> and (Na<sub>2</sub>O + K<sub>2</sub>O) values were recast as per 100% totals. The recast values (**Fig. 1**) range from  $46.55 < \text{SiO}_2 < 49.17$  and  $5.12 < (\text{Na}_2\text{O} + \text{K}_2\text{O}) < 5.67$  such that these samples plot in the silica undersaturated alkaline fields along the classification divide between Alkali Olivine Basalt and Hawaiite (Cox, Bell and Pankhurst, 1979; **Fig. 2**) or Basalt and Trachy basalt (LeBas, LeMaitre and Streckeisen, 1986). Additionally for this level of silica, the Al<sub>2</sub>O<sub>3</sub> values between 15.27-16.24 are well below the range expected for arc magmas or Hi-Al basalts, additionally confirming their within plate, alkaline character and plagioclase fractionation rather than any sort of crustal feldspar contamination (either at depth or by glacial materials). They are in the same unaltered and uncontaminated state as at the time of eruption.

4) For the AFM classification Triangle (Irvine and Baragar, 1971) the main distinction is between alkaline and tholeiitic iron enriched basalts versus calc-alkaline magmas. A is total alkalis (Na<sub>2</sub>O + K<sub>2</sub>O) and M is MgO and F is FeO\* (total iron as ferrous or total iron plus MnO plus Cr<sub>2</sub>O<sub>3</sub>) recast as 100%. The Kitasu Hill samples plot together among with Hawaiites and differentiated Alkali-Olivine Basalts with  $21.88 < A < 24.08$ ,  $18.84 < M < 20.09$  and  $56.14 < F < 59.28$ . The iron enrichment trend is comparable to world hawaiites but less than Icelandic lavas and more than any calc-alkaline lavas. This shows early olivine fractionation under dry low pressure conditions before magnetite forms (**Fig.1**).

5) The bulk major element chemistry is consistent with the modal mineralogy in having low pressure fractionation of plagioclase and olivine with 3-4 times more plagioclase than olivine as

phenocrysts. This suggests dry low pressure crystallization at the base of the crust which in this region is < 25 km from crustal refraction studies (Yuan, Spence and Hyndman, 1992) and <18 km from joint inversion of gravity and refraction data (Lowe and Dehler, 1995). This puts the asthenosphere directly beneath the crust and puts the mantle in the spinel peridotite stability field.

6) The high alkali values are partially due to low degrees of partial melting of a dry shallow upper mantle and partially due to early fractionation of Mg rich olivine and calcic plagioclase.

7) Comparing trace element values to more primitive basalts reveals the Kitasu Hill samples to be depleted in compatible elements:  $0.008 < \text{Cr}_2\text{O}_3 < 0.011$ ,  $40 < \text{Ni} < 46$ ,  $31.3 < \text{Co} < 35.7$  and moderately enriched in incompatible elements, especially those associated with low melt % or fractionated E-Morb, alkaline, within-plate settings, specifically:  $2.42 < \text{TiO}_2 < 2.5$ ,  $0.91 \text{ P}_2\text{O}_5 < 1.07$ ,  $353 < \text{Ba} < 375$ ,  $\text{Sr}$ ,  $19.2 < \text{Rb} < 29.3$ ,  $246.7 < \text{Zr} < 275.5$ ,  $36.7 < \text{La} < 39.2$ ,  $74.7 < \text{Ce} < 77.3$ .

8) Because some of the incompatible element enrichment trends vary inversely with silica, there is likely a bit of source heterogeneity or some kind of heterogeneity like layering in a deep crustal or subcrustal magma chamber. The tiny amount of fresh, unmelted granodiorite xenoliths do not seem to be adequate to account for much contamination or variation in incompatible elements. (e.g. batch extraction or minor source heterogeneity dominate over contamination to account for what little variation is present.)

9) These are simple, monogenetic, within-plate, small volume, dry, decompression melts like much of the within plate basalts for Miocene through Recent from the Cordillera. They are mantle derived, evolved at the base of the crust before erupted and show little if any indication of crustal contamination.

## Petrochemical Discriminant Diagrams

The following diagrams (Figs. 1 to 14) were plotted in R using GCDkit (Janousek et al., 2006). Symbols for all the figures are as follows: Sample 17-BJB-001= blue triangle (includes replicate samples); 17-BJB-002 = green diamond; 17-BJB-003 = black dot; 17-BJB-004 = red square.

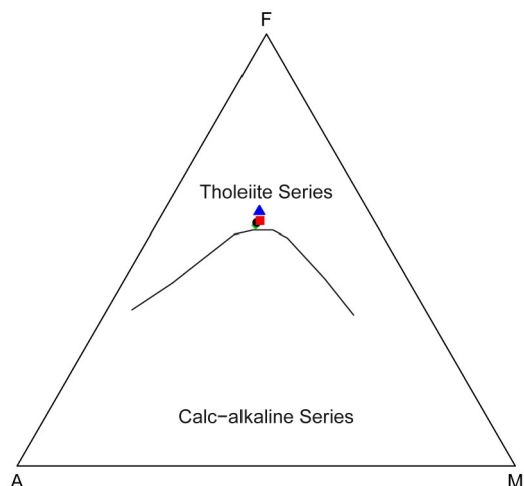


**Figure 1.** AFM Plot after Irvine and Baragar (1971) shows these basalts to be more ferrous than the Calc-alkaline-Tholeiite dividing line.

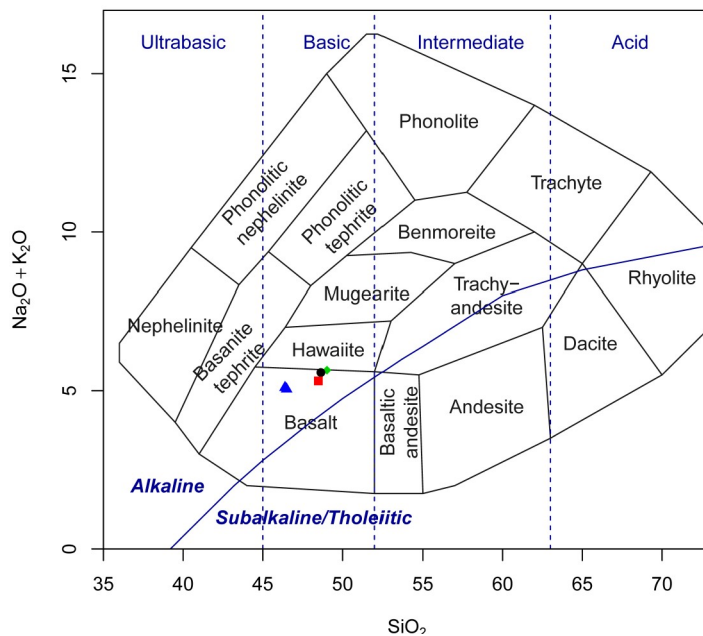


**Figure 2.** TAS Plot after Cox et al. (1979) show the Kitasu Hill Basalts to plot in the Alkaline field near the boundary between the Basalt (alkali Olivine Basalt) and Hawaiite subfields. Similar plots by Le Bas (1986) or Middlemost (1994) assigns the Kitasu Hill magmas to their Trachybasalt field.

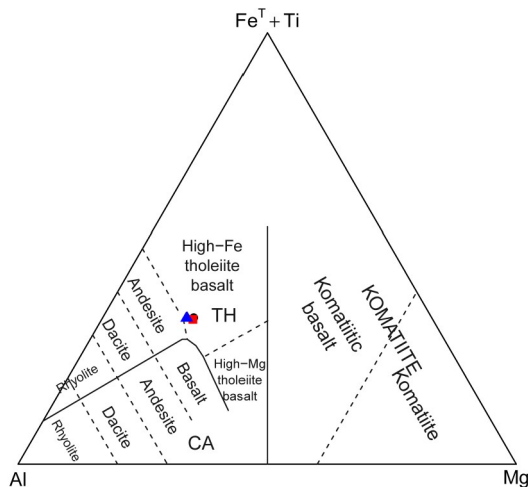


**Figure 3.** Al-(Fe<sup>T</sup> + Ti)-Mg plot of Jensen (1976) assigns the Kitasu Hill magmas to the High-Fe Tholeiite field.

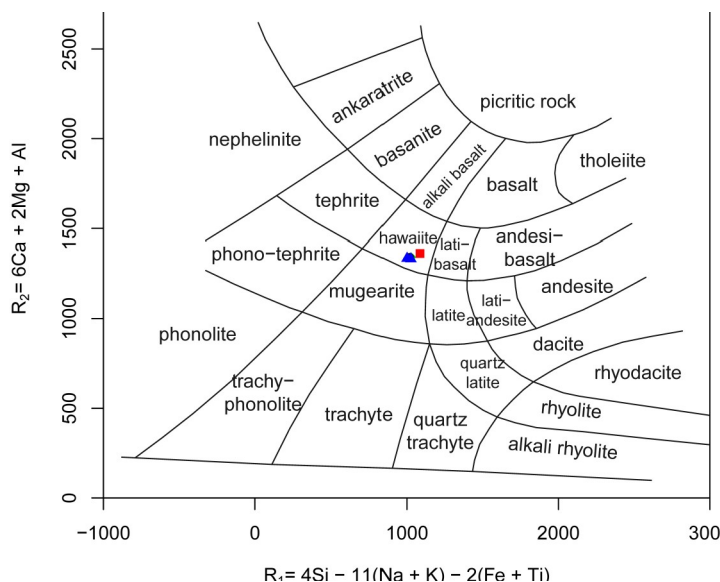


**Figure 4.** R2 vs R1 of De la Roche (1980) assigns the Kitasu Hill magmas to the Hawaiite field.



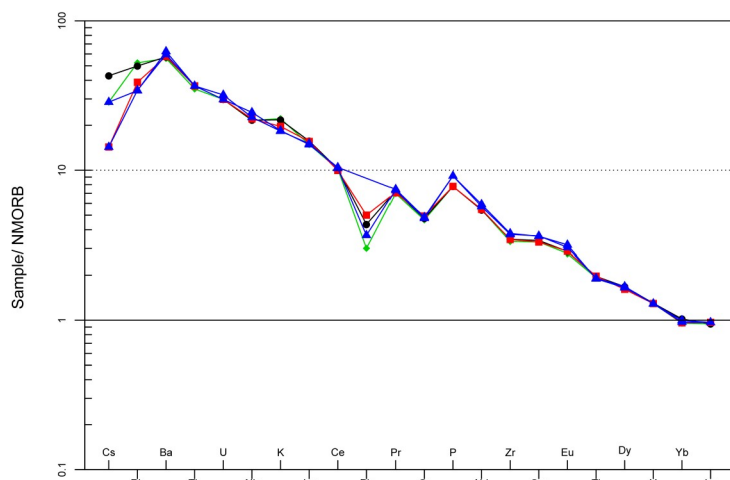


**Figure 5.** Spider plot normalized to N-Morb after Sun and McDonough, (1989) for Kitasu Hill lavas. There is progressive enrichment in LILE's (Large ion Lithophile Elements) to about 60 X N-Morb while Yb and Lu are unfractionated. This indicates fractionation in a deep magma chamber prior to eruption in keeping with low Mg#'s. Sr, Pb and Cs show variable depletion by up to a factor of 4 compared to adjacent elements. This

likely mirrors substantial plagioclase feldspar fractionation.

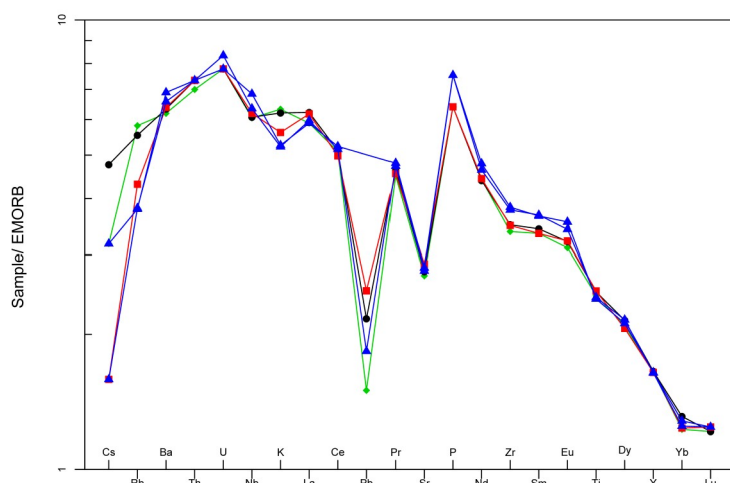


**Figure 6.** Spider plot normalized to E-Morb after Sun and McDonough (1989) for Kitasu Hill lavas. They mirror slightly enriched E-morbs for most elements and show enrichment in LILE's up to ~8 X due to deep fractionation. There is notable variable depletion in Cs, Pb and Sr likely due to substantial plagioclase feldspar fractionation. Slight relative enrichments in P and U compared to adjacent elements are likely a source effect due to elevated apatite or whitlockite in the mantle source or via

slight contamination from evolved plutonic crustal rocks in transit.

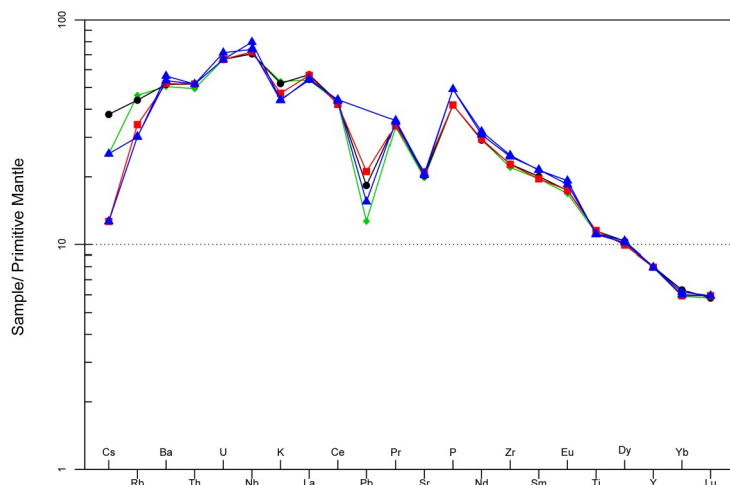


**Figure 7.** Spider plot normalized to Primitive Mantle after Sun and McDonough (1989) for Kitasu Hill lavas. They show 8 to 80 X enrichment compared to Primitive mantle showing derivation from a previously fractionated mantle source. The HREE's Nd-Lu along with High Field Strength elements Zr and Ti show 8-20 times enrichment while the LILE's show 40-80 X enrichment as a mantle source effect. Pb, Rb and Cs show variable depletion compared to

other LILE's suggesting plagioclase feldspar fractionation prior to eruption.

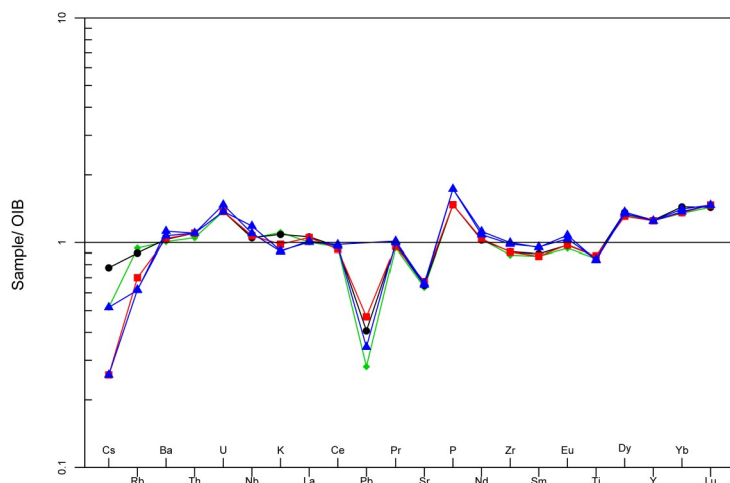


**Figure 8.** Spider plot normalized to OIB's (Ocean Island Basalt) after Sun and McDonough, (1989) for Kitasu Hill lavas. They are very much like late stage, low degrees of partial melting that generate alkaline OIB's. As with the other spider plots Pb and Cs indicate variable degrees of plagioclase feldspar fractionation.

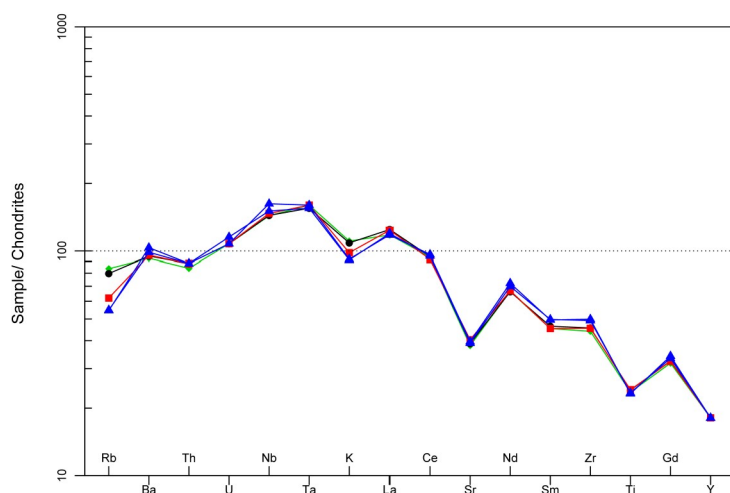


**Figure 9.** Spider plot normalized to chondrites after Sun et al. (1980) for Kitasu Hill lavas. They are tightly clustered with 20 to 200 X enrichment relative to chondrites with most LILE's around 100 X chondrite as an original source enrichment effect.

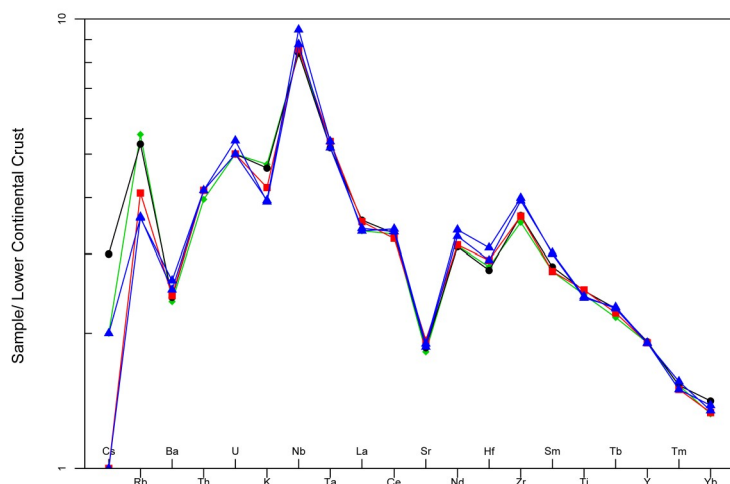


**Figure 10.** Spider plot normalized to Lower Continental Crust after Taylor and McLennan (1985) for Kitasu Hill lavas. They are tightly clustered with 1 to 10 X enrichment for all elements and 3 to 5 times enrichment for LILE's. Because primitive Kitasu Basalts differ so little from lower crust it is hard to rule out some contamination. However, the greater variation for K, Ba, Rb and Cs cannot be explained by lower crustal contamination and must be due to other source or fractionation effects.

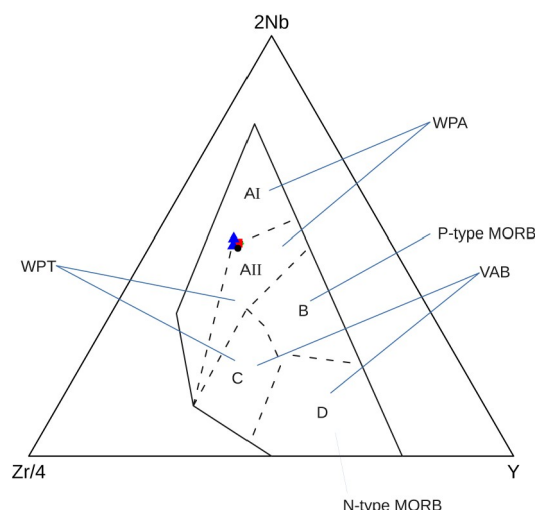


**Figure 11.** The Zr/4-2-Nb-Y discriminant plot of Meschede (1986) distinguishes basalt types according to their tectonic settings using the commonly analysed HFS elements. The Kitasu Hill Lavas plot on the boundary of the 2 alkaline within-plate basalt fields (AI and AII). This suggests post tectonic, low degrees of dry partial melting, and a within-plate setting.

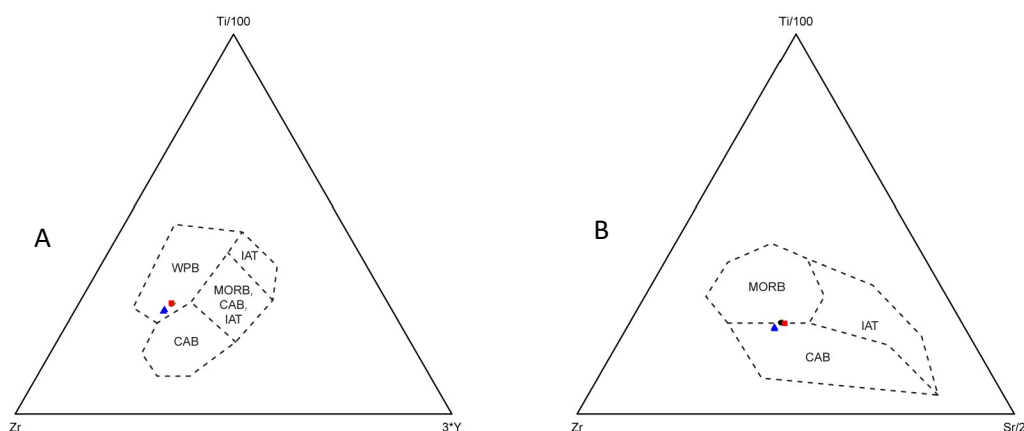


**Figure 12.** Basalt tectonic discriminant diagrams after Pearce and Cann (1973). A) The relative Y depletion of the Kitasu Hill lavas is a within plate signature. B) The Kitasu hill lavas straddle the MORB-CAB field boundary but this is less diagnostic as source composition and tectonic setting are not well discriminated for either low melt fraction alkaline basalts nor for within-plate basalts which is a better classification for Kitasu Hill as inferred from other discriminants.

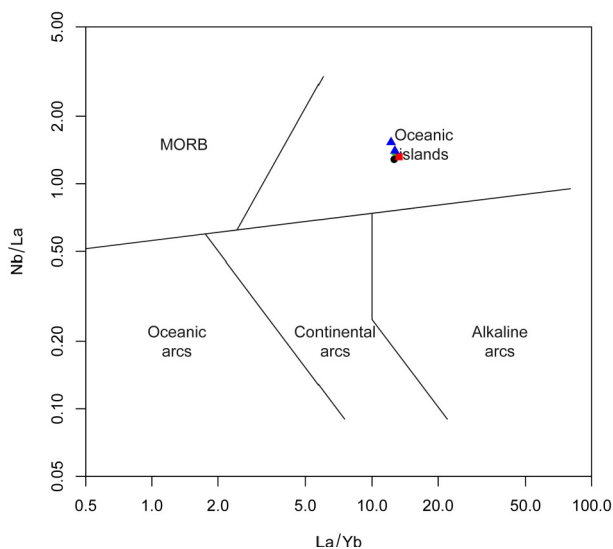


**Figure 13.** Basalt tectonic discriminant diagram Nb/La vs La/Yb after Hollocher et al. (2012). Kitasu lavas have Nb/La > 1.0 and well above the discriminant boundary for the arc rocks with characteristic Nb fractionation. The Kitasu lavas' high value for La/Yb > 12 is characteristic of alkaline basalts with low degrees of partial melting or substantial mantle source enrichment in LREE's. On this plot the Kitasu Hill lavas fall in the Ocean Island field.

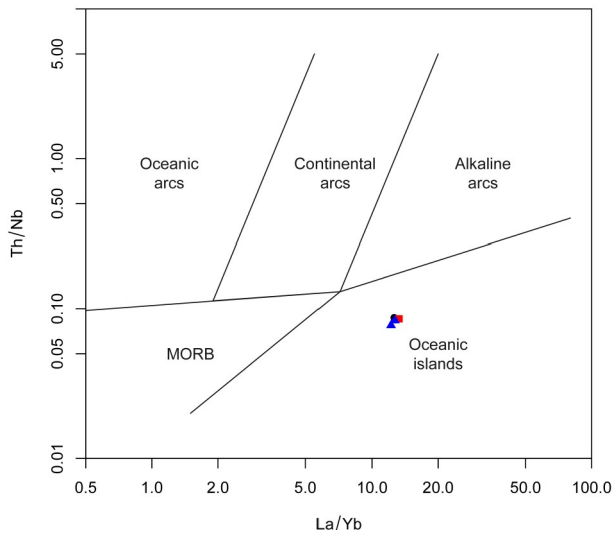


**Figure 14.** Basalt tectonic discriminant diagram Th/Nb vs La/Yb after Hollocher et al. (2012). Kitasu lavas have Low Th/Nb below 0.08 and La/Nb > 12 as for Ocean Island Basalts. This confirms their alkaline character, low degrees of partial melting and within plate setting. Low Th precludes any sedimentary source or contamination.

## Norm Calculations Kitasu Hill and Nearby Lavas

CIPW Vol% norms were calculated using IOGAS and  $\text{FeO}^*/\text{Fe}_2\text{O}_3$  of 0.6364 as per the average of 15 basalts from Woodsworth (1991) including seven from Kitkatla Inlet and Aristazabal Island and one from Steele Rock (WV sample numbers; Table 2). The 3 samples labelled SE-# were collected by Jack Souther and reported in Erdman's (1985) thesis and they came from Aristazabal, Kitasu and Lake Island and the final 2 SE-M# samples were calc alkaline basalts from the Masset Formation also reported by Erdman (1985).

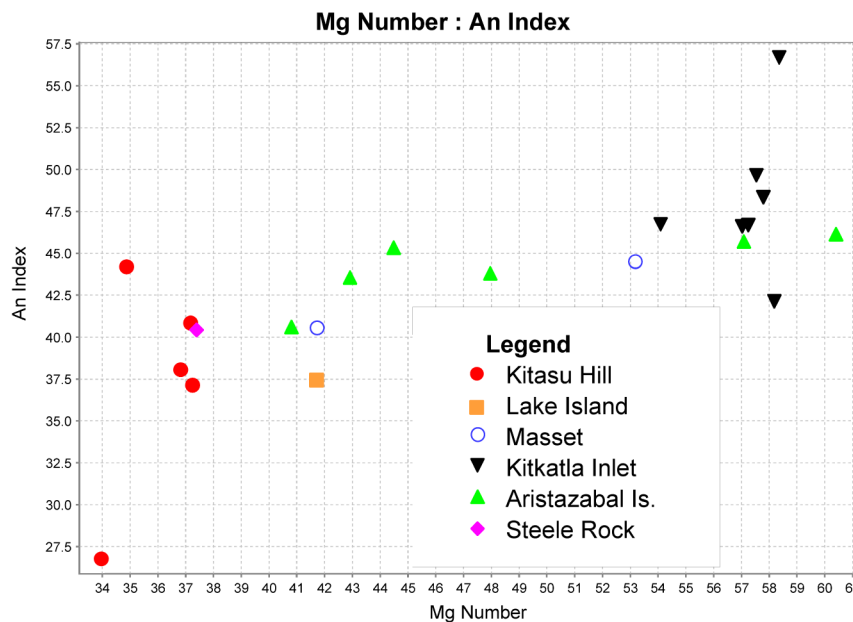


**Figure 15.** Mg number versus An index. Mg number is the molar ratio  $\text{MgO}/(\text{MgO}+\text{FeO}^*)$  where  $\text{FeO}^*$  is the total iron calculated as FeO. This estimates how Mg-rich or primitive an igneous rock is. An index is the Anorthite molar content  $\text{An}/(\text{An}+\text{Ab})$  or how calcic the plagioclase is.



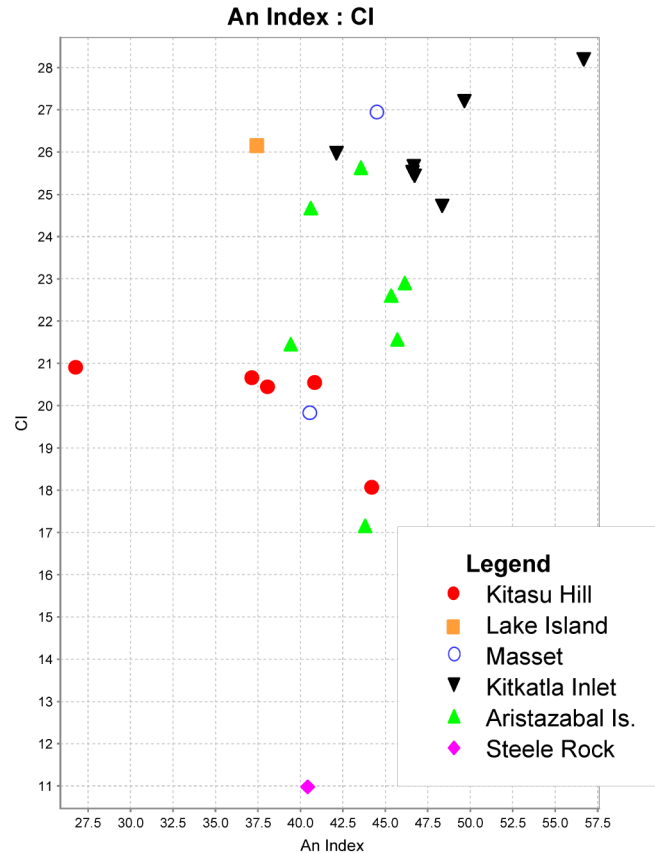


**Figure 16.** Normative colour index (CI) versus Anorthite index (An), where the normative CI= the sum of all ferromagnesium silicate minerals in the norm.

The Kitasu Hill Norms have no Quartz,  $7.93 < Or < 9.45$  and high values for titanomagnetite (= Mt+Ilm) of  $7.23 < TiMt < 7.56$  compared to other regional basalts and it reflects their enriched or evolved alkaline character. The high value for titanomagnetite corresponds to the low Mg#'s  $34.9 < Mg\# < 37.3$  (see graph Mg # versus Normative Plagioclase, An Index; **Fig. 15**) and is a sign of iron enrichment and deep fractionation of Mg rich olivine prior to eruption. The lavas are distinctive by geographic region also on An index versus normative colour index (Di+Hy+Ol; **Fig. 16**). On Ol-An-Di (from the haplo-basalt system; **Fig. 17**), all the regional lavas are olivine basalts. When normalized to total magnetite, the Kitasu samples have proportions of Pl:Px:Ol:TiMt of  $\sim 8:2:1:1$ . In that the Kitasu Hill lavas are quenched as glassy rocks with a few % phenocrysts, the norms calculation overestimate the total plagioclase and the total amount of iron titanium oxides. Given the petrographic order of crystallization of  $Pl > Ol > CPx > Mt$  the norms provide good agreement. Normative An% of the total plagioclase ranges from  $34.2 < An\% < 41.0$ . Actual plagioclase cores are more calcic and reflect crystallization at depth. High values for Apatite reflect the tholeiitic enrichment trend or source enrichment for these basalts. Compared to the nearby lavas from Hecate Strait, the norm calculations help to demonstrate 3-4 unique suites of closely related lavas but with slightly different source enrichment and fractionation prior to eruption. An additional check of the norm versus the mode and physical properties is to look at the densities, and magnetic susceptibilities. Samples 17-BJB-003 and 004 have several percent porosity and high grain densities due to the Fe content. They also had

magnetic susceptibilities of  $\sim 10^{-2}$  SI. On the Henkel plot a density of  $\sim 2.8$  and Si, indicate about 70% of the Q - non ferromagnesian minerals,  $\sim 29\%$  F - Ferromagnesian and 0.4% M – Magnetite (*see* Enkin, 2018). See QFC versus Vol% Magnetite (**Fig. 18**) where the lavas cluster by geographic groups due to different proportions of plagioclase to ferromagnesian minerals in the norm and slightly higher normative magnetite for the Kitasu lavas. The norms, assuming complete crystallization gave  $\sim 72:21:7$ . This confirms incomplete crystallization and an iron rich glass which behaved paramagnetically.

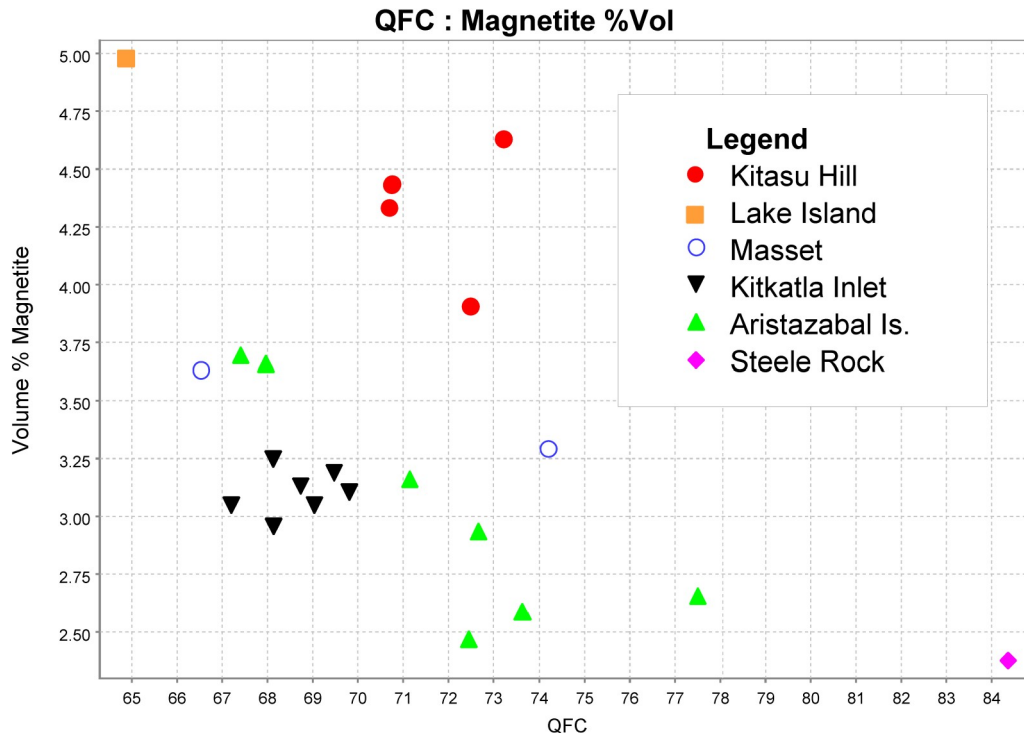


**Figure 17.** Plot of non ferromagnesian minerals (quartz, feldspars, calcite; QFC) versus percent volume of magnetite.

## References

- Cox, K.G., Bell, J.D. and Pankhurst, R. J., 1979. The Interpretation of Igneous Rocks; London University, London, 450 p., [doi.org/10.1007/978-94-017-3373-1](https://doi.org/10.1007/978-94-017-3373-1)
- De La Roche, H., Leterrier, J., Grandclaude, P., Marchal, M., 1980. A classification of volcanic and plutonic rocks using R1R2- diagram and major element analyses – its relationships with current nomenclature; Chemical Geology v. 29, p.183-210. doi: 10.1016/0009-2541(80)90020-0
- Enkin, R.J., 2018. Canadian rock physical property database: first public release; Geological Survey of Canada, Open File 8460, 1 .zip file. <https://doi.org/10.4095/313389>
- Erdman, L.R., 1985. Chemistry of Neogene basalts of British Columbia and the adjacent Pacific Ocean floor; a test of tectonic discriminant diagrams; M. Sc. Thesis, University of British Columbia, Vancouver, 294 p.

- Hollocher, K., Robinson, P., Walsh, E., Roberts, D., 2012. Geochemistry of amphibolite-facies volcanics and gabbros of the Storen Nappe in extensions west and southwest of Trondheim, western Gneiss region, Norway: a key to correlations and paleotectonic settings; *American Journal of Science*, v. 312, p. 357-416. doi:10.2475/04.2012.01
- Irvine, T.M., Baragar, W.R.A., 1971. A guide to the chemical classification of common volcanic rocks; *Canadian Journal of Earth Sciences*, v. 8, p. 523-548. doi: 10.1139/e71-055
- Janousek, V., Farrow, C.M., Erban, V., 2006. Interpretation of whole-rock geochemical data in igneous geochemistry: introducing Geochemical Data Toolkit (GCDkit); *Journal of Petrology*, v.47(6), p.1255-1259. doi: 10.1093/petrology/egl013
- Jensen, L.S., 1976. A new cation plot for classifying subalkalic volcanic rocks; Ontario Division of Mines, Miscellaneous Paper 66, p.1-21.
- Lebas, M.J., Lemaitre, R.W., Streckeisen, A. and Zanettin, B., 1986. A Chemical Classification of Volcanic-Rocks Based on the Total Alkali Silica Diagram; *Journal of Petrology* v. 27(3), p. 745-750.
- Lowe, C., and Dehler, S. A., 1995. Crustal thickness beneath the Queen Charlotte basin, Canada: results of a seismically constrained gravity inversion; *Journal of Geophysical Research*, v. 100, No. B12, p. 24, 331-24, 345, doi.org/10.1029/95JB01874
- Meschede, M., 1986. A method of discriminating between different types of mid-ocean ridge basalts and continental tholeiites with the Nb-Zr-Y diagram; *Chemical Geology*, v.56, p. 207-218. doi: 10.1016/0009-2541(86)90004-5
- Pearce, J. A., Cann, J.R., 1973. Tectonic setting of basic volcanic rocks determined using trace element analyses; *Earth and Planet Science Letters*, v.19, p.290-300. doi: 10.1016/0012-821X(73)90129-5
- Sun, S.S., Bailey, D.K., Tarney, J., Dunham, K., 1980. Lead isotopic study of young volcanic rocks from mid-ocean ridges, ocean islands and island arcs; *Philosophical Transactions of the Royal Society of London*, v. A297, p.409-445. doi:10.1098/rsta.1980.022410.1029/95RG00262
- Sun, S.S., McDonough, W.F., 1989. Chemical and isotopic systematics of oceanic basalts: implications for mantle composition and processes; *in* *Magmatism in Ocean Basins*, (eds) Saunders, A.D., Norry, M., Geological Society of London Special Publications, v.42, p.313-345.
- Taylor, S.R, McLennan, S.M., 1985. *The Continental Crust: Its Composition and Evolution*; Blackwell, Oxford, p.1-312.
- Taylor, S.R, McLennan, S.M., 1995. The geochemical evolution of the continental crust; *Reviews in Geophysics*, v.33, p.241-265. doi: 10.1029/95RG00262

- Woodsworth. G.J., 1991. Neogene to Recent volcanism along the east side of Hecate Strait, British Columbia; in *Evolution and Hydrocarbon Potential of the Queen Charlotte Basin, British Columbia*, Geological Survey of Canada. Paper 90-10, p. 325-335.
- Yuan, T., Spence, G.D., and Hyndman, R. D., 1992. Structure beneath Queen Charlotte Sound from seismic-refraction and gravity interpretations; *Canadian Journal of Earth Sciences*, v. 29(7), p.1509-1529, [doi.org/10.1139/e92-120](https://doi.org/10.1139/e92-120)





Appendix 3 Table 2

The first 4 samples are from this study BJB001-004 as per the previous geochemistry table.  
The Remaining 19 samples came from Woodsworth (1991) Table 2 and the last 2 of those are from Erdman's (1985) thesis.  
Sample 88-WV-9 had a typo reporting P2O5 as 4.11 rather than the correct 0.411 as it appears here.  
Sample SE-050365 had a typo for TiO2 misreporting it as 2.35 instead of 1.35 as corrected here to the original thesis analysis.  
The average FeO/Fe2O3 for the WV samples as analysed by wet chemistry was 0.6364. This ratio was used to for the norms presented here for all samples.  
In the norm calculations above the Red data block columns R-AB are Wt% CIPW norms from R. Columns AD-An in green are IOGAS Vol% norms.  
Columns AO-AY in Black are Wt% CIPW norms from IOGAS. The Blue columns AZ-BJ are the differences of the Wt% norms from R-IOGAS and show good agreement to the second decimal place confirming the consistency of both programs. The IOGAS Vol% norm is recopied to the table below to correspond more readily to the petrography of the BJB samples.

Sample	SiO2_pct	Al2O3_pct	Fe2O3*_pct	FeO*_pct	MgO_pct	CaO_pct	Na2O_pct	K2O_pct	TiO2_pct	P2O5_pct	MnO_pct	Cr2O3_pct	ZrO2_pct
17-BJB-001	47.16	16.51	5.57	9.74	4.46	7.59	3.84	1.34	2.46	1.09	0.21	0.01	0
17-BJB-002	48.98	15.26	5.22	9.13	4.64	7.58	4.05	1.60	2.44	0.91	0.20	0.01	0
17-BJB-003	48.59	15.35	5.34	9.34	4.65	7.55	4.01	1.57	2.49	0.91	0.20	0.01	0
17-BJB-004	48.45	15.61	5.31	9.30	4.71	7.69	3.89	1.42	2.50	0.91	0.21	0.01	0
87WV-90a	49.76	15.76	3.94	6.90	8.21	8.44	3.92	0.97	1.52	0.38	0.16	0.04	0
87WV-91a	49.36	17.01	3.60	6.30	7.30	10.46	3.95	0.49	1.09	0.24	0.16	0.02	0
87WV-92	49.23	16.99	3.76	6.59	7.72	9.28	3.77	0.54	1.60	0.34	0.16	0.03	0
87WV-115	50.16	16.51	3.69	6.45	7.33	9.30	3.80	0.63	1.56	0.39	0.16	0.03	0
87WV-116	49.45	16.85	3.88	6.79	6.84	9.94	3.96	0.49	1.28	0.33	0.17	0.01	0
87WV-117	49.98	16.43	3.78	6.61	7.57	9.05	3.79	0.58	1.64	0.36	0.17	0.04	0
87WV-120	49.09	17.25	3.68	6.44	7.71	10.90	3.10	0.44	0.97	0.23	0.16	0.03	0
88WV-8	57.48	17.73	3.00	5.24	2.68	6.13	4.37	1.48	1.23	0.44	0.19	0.01	0
88WV-9	51.00	17.39	3.04	5.32	6.95	9.44	3.89	1.11	1.14	0.48	0.19	0.04	0
88WV-9	50.39	17.88	3.19	5.58	6.35	9.54	4.23	0.78	1.42	0.42	0.20	0.01	0
88WV-11	50.56	15.44	4.41	7.72	4.97	9.60	3.84	0.64	2.20	0.40	0.19	0.02	0
88WV-12	50.64	16.78	3.82	6.69	4.59	9.98	3.97	0.70	2.11	0.51	0.19	0.02	0
88WV-13	50.09	15.28	4.38	7.67	4.52	9.94	4.03	0.72	2.54	0.61	0.20	0.02	0
88WV-14	51.04	18.43	3.28	5.75	4.53	9.01	4.39	1.00	1.74	0.64	0.16	0.03	0
SE-090265	50.37	16.53	3.60	6.30	6.46	8.64	4.33	1.07	1.85	0.69	0.15	0.01	0
SE-050365	50.65	15.33	4.80	8.40	7.70	7.70	5.32	1.57	1.36	0.97	0.19	0.01	0
SE-030865	47.24	13.91	5.89	10.31	6.31	8.00	3.86	0.96	2.51	0.81	0.20	0.01	0
SE-M1	50.38	15.28	4.35	7.61	7.39	8.08	3.58	1.10	1.54	0.47	0.22	0.01	0
SE-M2	53.31	16.13	4.01	7.02	4.30	7.78	4.18	0.89	1.68	0.53	0.17	0.01	0

Sample SE-050365 from Erdman 1985 is more differentiated, more silica rich, lower in Mg, Fe total, Ti, and higher in Na and K

Green cells are over Hy not Ol																		Blue Cells have Ne in Norm			
																		Henkel Parameters			
																		Normalized			
																		P/Ol			
																		Ti=			
																		Px=O			
																		Px=O			
																		Px=O			
																		Px=O			
																		Px=O			
																		Px=O			
																		Px=O			
																		Px=O			
																		Px=O			
																		Px=O			
																		Px=O			
																		Px=O			
																		Px=O			
																		Px=O			
																		Px=O			
																		Px=O			
																		Px=O			
																		Px=O			
																		Px=O			
																		Px=O			
																		Px=O			
																		Px=O			
																		Px=O			
																		Px=O			
																		Px=O			
																		Px=O			
																		Px=O			
																		Px=O			
																		Px=O			
																		Px=O			
																		Px=O			
																		Px=O			
																		Px=O			
																		Px=O			
																		Px=O			
																		Px=O			
																		Px=O			
																		Px=O			
																		Px=O			
																		Px=O			
																		Px=O			
																		Px=O			
																		Px=O			
																		Px=O			
																		Px=O			
																		Px=O			
																		Px=O			
																		Px=O			
																		Px=O			
																		Px=O			
																		Px=O			
																		Px=O			
																		Px=O			
																		Px=O			
																		Px=O			
																		Px=O			
																		Px=O			
																		Px=O			
																		Px=O			
																		Px=O			
																		Px=O			
																		Px=O			
																		Px=O			
																		Px=O			
																		Px=O			
																		Px=O			
																		Px=O			
																		Px=O			
																		Px=O			
																		Px=O			
																		Px=O			
																		Px=O			
																		Px=O			
																		Px=O			
																		Px=O			
																		Px=O			
																		Px=O			
																		Px=O			
																		Px=O			
																		Px=O			
																		Px=O			
																		Px=O			
																		Px=O			
																		Px=O			
																		Px=O			
																		Px=O			
																		Px=O			
																		Px=O			
																		Px=O			
																		Px=O			
																		Px=O			
																		Px=O			
																		Px=O			
																		Px=O			
																		Px=O			
																		Px=O			
																		Px=O			
																		Px=O			
																		Px=O			
																		Px=O			
																		Px=O			
																		Px=O			
																		Px=O			
																		Px=O			
																		Px=O			
																		Px=O			
																		Px=O			
																		Px=O			
																		Px=O			
																		Px=O			
																		Px=O			
																		Px=O			
																		Px=O			
																		Px=O			
																		Px=O			
																		Px=O			
																		Px=O			
																		Px=O			
																		Px=O			
																		Px=O			
																		Px=O			
																		Px=O			
																		Px=O			
																		Px=O			
																		Px=O			
																		Px=O			
																		Px=O			
																		Px=O			
																		Px=O			
																		Px=O			
																		Px=O			
																		Px=O			
																		Px=O			
																		Px=O			
																		Px=O			
																		Px=O			
																		Px=O			
																		Px=O			
																		Px=O			
																		Px=O			
																		Px=O			
																		Px=O			
																		Px=O			
																		Px=O			
																		Px=O			
																		Px=O			
																		Px=O			
																		Px=O			
																		Px=O			
																		Px=O			
																		Px=O			
																		Px=O			
																		Px=O			
																		Px=O			
																		Px=O			
																		Px=O			
																		Px=O			
																		Px=O			
																		Px=O			
																		Px=O			
																		Px=O			
																		Px=O			
																		Px=O			
																		Px=O			
																		Px=O			
																		Px=O			
																		Px=O			
																		Px=O			
																		Px=O			
																		Px=O			
																		Px=O			
																		Px=O			
																		Px=O			
																		Px=O			
																		Px=O			
																		Px=O			
																		Px=O			
																		Px=O			
																		Px=O			
																		Px=O			
																		Px=O			
																		Px=O			
																		Px=O			
																		Px=O			
																		Px=O			
																		Px=O			
																		Px=O			
																		Px=O			
																		Px=O			
																		Px=O			
																		Px=O			
																		Px=O			
																		Px=O			
																		Px=O			
																		Px=O			
																		Px=O			
																		Px=O			
																		Px=O			
																		Px=O			
																		Px=O			
																		Px=O			
																		Px=O			
																		Px=O			
																		Px=O			
																		Px=O			
																		Px=O			
																		Px=O			
																		Px=O			
																		Px=O			
																		Px=O			
																		Px=O			
																		Px=O			
																		Px=O			